DISSERTATION

CARDIAC COMPUTED TOMOGRAPHY IN DOGS:

INSIGHTS INTO STRUCTURAL IMAGING AND THERAPEUTICS

Submitted by

I-Jung Bernard Chi

Department of Clinical Sciences

In partial fulfillment of the requirements

For the Degree of Doctor of Philosophy

Colorado State University

Fort Collins, Colorado

Spring 2025

Doctoral Committee:

Advisor: Brian Scansen
Co-Advisor: E. Christopher Orton

Lance Visser
David Bark

ABSTRACT

CARDIAC COMPUTED TOMOGRAPHY IN DOGS: INSIGHTS INTO STRUCTURAL IMAGING AND THERAPEUTICS

Visualization of intracardiac structures with medical imaging has always been a formidable task due to the inherently complex structure of mammalian hearts. Traditional two-dimensional (2D) imaging such as fluoroscopy and 2D echocardiography present challenges in reconstructing the three-dimensional (3D) morphology of cardiac structures and alterations in intracardiac architecture caused by cardiovascular disease. Challenges in accurately visualizing complex cardiac geometry can lead to incomplete or inaccurate assessments during surgical and transcatheter interventions. To overcome this issue, cross-sectional imaging such as cardiac computed tomography (CCT) may be utilized to allow a comprehensive, dynamic, and 3D evaluation of cardiac valves, chambers and major vascular structures.

One potential application of 3D imaging is preprocedural prediction of optimal fluoroscopic projections that can be used for intraprocedural guidance of cardiac interventions. For any given cardiac structure, there is an infinite number of 2D projections orthogonal to the straight-on (*en face*) projection forming a 360-degree circle of perpendicularity. The circle of perpendicularity becomes an arch of perpendicularity when considering projections above the fluoroscopic table only. In Chapter 1, this concept was explored by identifying the *en face* projections of various cardiac structures on CCT. The arch of perpendicularity (also known as the S curve) can be derived by using a trigonometric formula to solve the spatial relationship between the *en face* and perpendicular projections. Once the S curves are established, the optimal

fluoroscopic projections (OFPs) can then be characterized and used to guide cardiac interventions. Cardiac computed tomography studies from eighteen healthy dogs were used to generate S-curves and OFPs for selected cardiac structures. The projections were defined by the cranial-caudal angulation and left-right rotation angles of the C-arm assuming the dog is in dorsal recumbency. Mean OFP S-curves and 95% confidence curve areas were determined for the aortic, mitral, and pulmonary valve along with interatrial septum. The impact of thoracic conformation on OFPs was found to be non-significant.

By analyzing the CCTs from 18 dogs with severe pulmonary stenosis, the S-curves and OFPs of the pulmonary valve were described in Chapter 2. The coordinates of those optimized projections were found to be different from those of healthy dogs. Cardiac computed tomography from dogs with pulmonary stenosis were also used as a reference to examine the accuracy of pulmonary annular diameters measured on transthoracic echocardiography and angiocardiography. It was found that transthoracic echocardiography underestimates pulmonary annular diameter. Angiographic pulmonary annular diameters on standard lateral projection were also shown to be less precise when compared to the measurements made on CCT-derived OFPs.

The inodilator pimobendan has been shown to delay the onset of congestive heart failure and decrease cardiac mortality in dogs with degenerative mitral valve disease. The benefit of pimobendan may go beyond its effect on cardiac contractility and vasodilation. In Chapter 3, CCTs from 20 dogs with subclinical degenerative mitral valve disease were used to investigate the effects of pimobendan on mitral annular dynamics. By comparing the mitral annular dynamics before and after the administration of pimobendan, it was shown that pimobendan augmented the systolic contraction of the mitral annulus which likely reduced the regurgitant orifice area and severity of mitral regurgitation.

In conclusion, integration of CCT into clinical practice enhances our ability to evaluate and treat structural heart disease. Cardiac computed tomography can also be used as a reference to refine other imaging techniques and investigate the mechanism of action underlying various cardiovascular therapies.

ACKNOWLEDGEMENTS

I am extremely grateful for the support of my advisors Drs. Brian Scansen and Christopher Orton. Their determination to push the boundary of veterinary medicine inspired the work in this dissertation. I want to thank Dr. Lance Visser for sharing his wisdom in cardiology, academic career, and life. I would also like to thank my out-of-department committee member Dr. David Bark for providing insights from another scientific discipline. I appreciate Boehringer Ingelheim Animal Health and Colorado Clinical and Translational Science Institute Pilot Study Grant for sponsoring the research project associated with pimobendan in Chapter 3.

Dr. Marisa Ames took me under her wings and nurtured me in the early days of my career at CSU. I could never become the person I am today without her help.

Mrs. June Boon introduced me to the world of echocardiography and cardiology. June is the most influential mentor and friend anyone could ask for.

I would like to thank Dr. Brianna Potter for being an impeccable colleague and a kindred friend. It's been a pleasure to work alongside her and her precious canine child Gus since our paths collided at CSU.

I am extremely fortunate to have encountered the two best residentmates in this world. Drs. Evan Ross and Bruna Del Nero are my chosen siblings, and I will always cherish our everlasting friendship and support for each other.

Finally, I am forever thankful for the encouragement and utmost faith from my family and friends in both the United States and Taiwan.

DEDICATION

To my parents Chih-Chiang Chi and Man-Fei Liaw – Thank you for your unconditional love.

To my brother I-Jui Chi and sister in-law Yu-Fen Lin – Thank you for keeping me company.

To all my friends in Taiwan and the United States – I am fortunate to have you in my life.

To my pets in the past – Yoshi, Nana, Jolin, and Kiki – I will never forget about you. Thank you for coming into my life.

To all my patients and their families – Thank you for entrusting me and showing me the unbreakable bond between human and their companion animals. You've made me a better doctor, care giver, and person.

TABLE OF CONTENTS

ABSTRACT....ii
ACKNOWLEDGMENTS....v
DEDICATION....vi
CHAPTER 1 - OPTIMIZING FLUOROSCOPIC PROJECTIONS FOR THE CANINE HEART USING CARDIAC COMPUTED TOMOGRAPHY....1
1.1 Introduction....1
1.2 Material and method....2
1.2.1 *Animals and study design*....2
1.2.2 *Thoracic radiographs and thoracic conformation*....3
1.2.3 *Cardiac computed tomography*....3
1.2.4 *Optimized fluoroscopic projections and S curves*....4
1.2.5 *Statistics*....5
1.3 Results....6
1.3.1 *Optimized projections of the aortic valve*....6
1.3.1.1 *Cusp overlap view*....6
1.3.1.2 *Coplanar view*....7
1.3.1.3 *Coronary artery views*....7
1.3.2 *Optimized projections of the mitral valve*....7
1.3.2.1 *Two-chamber view (Intercommissural view)*....8
1.3.2.2 *Three-chamber view (Inflow-outflow view*)....9
1.3.2.3 *Four-chamber view*....9
1.3.3 *Optimized projections of the pulmonary valve*....9
1.3.3.1 *Cusp overlap view*....10
1.3.3.2 *Coplanar view*....10
1.3.4 *Optimized projections of the interatrial septum*....10
1.3.4.1 *Bicaval view*....11
1.3.4.2 *Short axis view of the interatrial septum*....11
1.3.5 *Effect of thoracic conformation on optimized fluoroscopic projections*....11
1.4 Discussion....11
1.5 Conclusion....15
TABLES AND FIGURES – CHAPTER 1....16
REFERENCES – CHAPTER 1....26
CHAPTER 2 - CHARACTERIZATION OF OPTIMIZED FLUOROSCOPIC PROJECTIONS OF THE PULMONARY VALVE IN DOGS WITH PULMONARY STENOSIS USING CARDIAC COMPUTED TOMOGRAPHY....31
2.1 Introduction....31
2.2 Material and method....32
2.2.1 *Case selection*....32
2.2.2 *Cardiac computed tomography – Image acquisition*....32
2.2.3 *Cardiac computed tomography – Image analyses*....34

2.2.4 *Optimized fluoroscopic curve (S curve) of the pulmonary valve*....35
2.2.5 *Transthoracic echocardiography*....35
2.2.6 *Angiocardiography*....36
2.2.7 *Statistics*....36
2.3 Results....37
2.3.1 *Study group characteristics*....37
2.3.2 *Comparing optimized fluoroscopic projections of the pulmonary valve*....37
2.3.3 *Bland-Altman analyses on different pulmonary annular measurements*....38
2.4 Discussion....38
2.5 Conclusion....41
TABLES AND FIGURES – CHAPTER 2....42
REFERENCES – CHAPTER 2....49
CHAPTER 3 - EFFECTS OF PIMOBENDAN ON MITRAL ANNULAR DYNAMICS AND SEVERITY OF MITRAL REGURGITATION IN DOGS WITH SUBCLINICAL DEGENERATIVE MITRAL VALVE DISEASE AS DETERMINED BY CARDIAC COMPUTED TOMOGRAPHY....52
3.1 Introduction....52
3.2 Material and method....53
3.2.1 *Animals and study design*....53
3.2.2 *Echocardiography*....54
3.2.3 *Cardiac computed tomography – Image acquisition*....54
3.2.4 *Cardiac computed tomography – Image analysis*....55
3.2.5 *Statistics*....57
3.3 Results....57
3.3.1 *Study sample*....57
3.3.2 *The effect of pimobendan on mitral annular dynamics*....58
3.3.3 *The effect of pimobendan on mitral regurgitation and left heart volumes*....58
3.3.4 *The effect of pimobendan on estimates of LV afterload*....58
3.4 Discussion....59
3.5 Conclusion....62
TABLES AND FIGURES – CHAPTER 3....63
REFERENCES – CHAPTER 3....70
CHAPTER 4 – CONCLUSION AND FUTURE DIRECTIONS....75
LIST OF ABBREVIATIONS....77

CHAPTER 1: OPTIMIZING FLUOROSCOPIC PROJECTIONS FOR THE CANINE HEART USING CARDIAC COMPUTED TOMOGRAPHY

1.1 Introduction

Visualization of cardiac anatomy by two-dimensional imaging is complicated by the inherently complex structure of mammalian hearts. Fluoroscopy is used as the principal imaging modality when performing transcatheter cardiac intervention (TCI) in which the operator can set the left/right anterior oblique (LAO/RAO) rotation and cranial/caudal (CRA/CAU) angulation of the C-arm to achieve desired views of the heart. However, fluoroscopic guidance during veterinary TCI is often defaulted to standard lateral or ventrodorsal projections of the thorax and not optimized for the cardiac structure of interest (SOI). Such practice can create parallax of the SOI making it challenging for the interventionalist to recognize anatomic landmarks or accurately measure the SOI. To resolve this issue, the X-ray beam should be positioned orthogonally to the SOI's central trajectory or *en face (facing the valve*) projection [1–4]. The resultant projections are defined as optimal fluoroscopic projections (OFPs) of the SOI, which are determined by the three-dimensional orientation of the SOI rather than how the patient is positioned on the fluoroscopy table.

Cardiac computed tomography (CCT) has become a critical imaging modality for pre-planning of TCI in people due to its ability to deliver high-resolution, three-dimensional imaging of the beating heart [5]. In addition to evaluation of landing zone anatomy and device sizing, imaging planes equivalent to the *en face* and OFPs in double-oblique multiplanar reformatting (MPR) can be created and used to predict intraoperative C-arm positions during the procedure (assuming the human subject is in supine position) [1–3,6,7]. Even with the increasing utilization

of CCT technology in veterinary cardiology, the use of CCT to determine OFP for a patient has not, to the authors' knowledge, been reported in veterinary cardiology.

Variation in body size and shape across individual animals has always been a major challenge for veterinary diagnostic imaging. Chest conformation can affect the anatomic orientation of the heart relative to the chest walls and change how the heart is projected onto a two-dimensional imaging system such as fluoroscopy. For this reason, thoracic conformation has been considered a major variable in radiographic measurement of heart size in dogs [8,9]. Is it not known whether thoracic conformation shares the same influence on OFPs across dogs with different body shapes.

The primary objective of this study was to explore and characterize non-standard fluoroscopic projections optimized for selected cardiac SOIs using CCT. The effect of thoracic conformation on OFP coordinates was also examined.

1.2 Material and method

1.2.1 Animals and study design

Healthy, staff- and student-owned dogs were prospectively recruited at the Colorado State University Veterinary Teaching Hospital (**Table 1**). Inclusion criteria included the absence of major abnormalities on physical examination, normal blood pressure measurement, normal thoracic radiographs, unremarkable blood work (complete blood count and chemistry profile), and a structurally normal heart on a comprehensive echocardiography study. The dogs were excluded if they were receiving any medications with potential cardiovascular effect. After the screening diagnostics, a sedated CCT was acquired on each dog according to the protocol below. Following full recovery from sedation, the dog was discharged to its owner and no further intervention or

follow-up was performed. The study protocol was approved by the Institutional Animal Care and Use Committee at Colorado State University (protocol number: 1039).

1.2.2 Thoracic radiographs and thoracic conformation

Right lateral, left lateral, and ventrodorsal thoracic radiographs were acquired to screen for cardiovascular, respiratory, or other intrathoracic pathologies. Thoracic depth (TD) and thoracic width (TW) were measured on thoracic radiographs and the TD-to-TW ratio (TD:TW) was calculated on each dog as a measure of chest conformation [8,9]. Thoracic depth was measured on a right lateral radiograph from the cranial edge of the xiphoid process to the ventral border of the vertebral column along a line perpendicular to the vertebral column. Thoracic width was measured on the ventrodorsal radiograph as the linear dimension between the medial borders of the eighth ribs at their most lateral curvatures (**Figure 1**). The dogs in the study were then divided equally into a narrow chest (TD:TW above median) and wide chest (TD:TW below median) group.

1.2.3 Cardiac computed tomography

A dual source, 384-slice (192 slices in each detector row) computed tomography scanner (SOMATOM Force Dual Source CT scanner, Siemens Medical Solutions, Malvern, PA, USA) was used to acquire all CCT studies. The CCT studies were acquired under brief sedation and spontaneous respiration. The sedation protocol was standardized and monitored by the Anesthesia and Pain Management Service at the authors' institution. All dogs received 0.2 to 0.5 mg/kg butorphanol IV, followed by 1 to 2 mg/kg alfaxalone IV titrated to a sufficient level of sedation to enable the dog to lie still for 5 to 10 minutes. Once sedate, the dog was positioned on the CT table in ventral recumbency. Pulse rate and peripheral oxygen saturation were monitored by pulse oximetry with heart rate and rhythm monitored by ECG. Flow-by oxygen was supplemented throughout the scan.

After topograms, a pre-contrast thoracic CT was acquired and reconstructed to select the desired monitoring slice. In the first two dogs, the region of interest with a threshold of 150 Hounsfield units was placed in the pulmonary trunk or cranial vena cava for the dextrophase, and the levophase was acquired after 5 to 6 seconds depending on the heart rate. For all other dogs, the region of interest was placed in the aortic arch to trigger the levophase and then the dextrophase was acquired after 8 to 12 seconds depending on the heart rate. Two retrospectively gated CCT scans were acquired for each dog. A triphasic contrast (Omnipaque™, GE Healthcare, Chicago, IL, USA) protocol delivering a total of 1.5 mL/kg contrast was used: 1 mL/kg of 100% contrast at 2 to 4 ml/s, followed by 1 mL/kg of 50% contrast-to-saline mixture at 2 to 4 ml/s, and a final 1 mL/kg saline bolus at 2 to 4 ml/s. The contrast injection rate was variable according to the body weight of the patient, with an average and standard deviation of 0.16 +/- 0.06 ml/s/kg. All studies were reconstructed at 0.75 mm slice thickness with the field-of-view containing the entire heart and great vessels. Both the levophase and dextrophase scans were reconstructed into 20 phases at 5% increments of the R-to-R cycle length and stored for further analysis.

1.2.4 Optimized fluoroscopic projections and S curves

Selected heart valves (aortic, mitral, and pulmonary) and the interatrial septum were segmented to locate the *en face* projections using a research imaging program (FluoroCT, version 3.2, Circle Cardiovascular Imaging Inc., Calgary, Canada). There are an infinite number of OFPs perpendicular to the *en face* of a SOI, and a trigonometric formula was used to describe the three-dimensional arch of OFPs [4,6]:

$$\phi = -\arctan\frac{\cos(\theta - \theta_{en\,face})}{\tan\phi_{en\,face}}$$

Where the angulation ($\phi_{en\,face}$) and rotation ($\theta_{en\,face}$) of the *en face* is known, the CRA/CAU angulation (ϕ) of the OFP is determined by its LAO/RAO rotation (θ). This

trigonometric relationship represents an infinite number of projections perpendicular to the *en face* projection, which can then be plotted onto a geographic coordinate system (consider LAO/RAO rotation as the longitude and CRA/CAU angulation as the latitude) to generate the optimized projection curve or 'S curve' due to its s shape. The OFPs of each structure are identified on the S curve to visualize certain perspectives of the SOI. All projections are defined by their LAO/RAO rotation and CRA/CAU angulation in degrees assuming the dog is in dorsal recumbency.

1.2.5 Statistics

All continuous variables were examined for normality using the Shapiro-Wilk test. Student's t-test or Wilcoxon rank-sum test was used for parametric and non-parametric comparison of means/medians. Statistical methods described in directional statistics were used to analyze the C-arm rotation (LAO/RAO) and angulation (CRA/CAU) as geographical coordinates [10]. For each sample of spherical coordinates, von Mises-Fisher distribution was evaluated with visual inspection of longitude and co-latitude plots. The mean S curves and 95% confidence curve areas of each SOI were generated from the means and 95% cones of confidence of their *en face* coordinates. The 95% cone of confidence was calculated from the 95% deviation angle of each spherical coordinate sample. Mean *en face* and OFPs of the narrow- and wide-chest groups were compared using the two-sample Watson-Williams test. The significance level (alpha) of the study was 0.05. Statistical analyses and graphics of the spherical statistics were compiled using a proprietary programming language and computing environment (MATLAB R2024b, The MathWorks, Inc., Natick, MA, USA). The standard statistics were computed using an open-source programming language and software environment (R version 4.4.1 [Race for your life]; RStudio version 2024.09.0+375, Posit Software, Boston, MA, USA).

1.3. Results

1.3.1 Optimized projections of the aortic valve

The aortic valve (AV) apparatus consists of three leaflets (non-, right-, and left-) and corresponding sinuses of Valsalva that join the ascending aorta at the sinotubular junction (STJ). With respect to nomenclature, we favor the construct that a leaflet is a discrete subsegment of the valve, a sinus is the virtual space behind a leaflet, and a cusp refers to the two together – a leaflet with its associated sinus [11]. Moreover, the common perception of the aortic annulus as a "virtual" ring that connects the three nadirs of the AV cusps is inaccurate. In reality, the "true" annulus that consists of the entire attachment of all three leaflets and functions as the ventriculo-aortic junction forms a crown-like structure [3]. The virtual AV annulus is a dynamic ring that is more circular in systole and elliptical in diastole [7]. When optimizing fluoroscopic projections for the AV, the OFPs will each have the AV annulus in-plane, though with different configurations of the cusps and coronary ostia.

Reports of AV intervention in dogs are limited. This is likely due the low prevalence of congenital/acquired aortic valvar disease and the fact no transcatheter intervention has been reported to prolong survival in subvalvar aortic stenosis [12]. The role of transcatheter AV implantation/replacement in dogs remains to be investigated. Regardless, four proposed projections mirroring clinical experience in people may potentially be useful in the setting of AV intervention for dogs (**Figures 2A**, **3**, and **4**):

1.3.1.1 Cusp overlap view

By overlapping the left and non-coronary cusps to isolate the right coronary cusp, the aortic annulus is viewed in its minor dimension with the AV and mitral valves fully separated (**Figure 3A**). This projection requires lateral rotation with mild cranial or caudal angulation

(**Figure 2A**, **Table 2**). This particular OFP provides visualization of the full length of the left ventricular outflow tract and the atrioventricular conduction axis locating between the non- and right aortic cusps.

1.3.1.2 Coplanar view

In the coplanar view of the AV (**Figure 3B**), the nadirs of all three cusps are connected to form a straight line (the virtual annulus) with central positioning of the right cusp. This view gives the major dimension of the AV annulus with a foreshortened left ventricular outflow tract. This projection is in proximity to the standard ventrodorsal projection with slight cranial angulation (**Figure 2A**, **Table 2**).

1.3.1.3 Coronary artery views

Coronary arterial diseases are rare in dogs, but coronary anomalies or malformations may occasionally require cardiac catheterization for diagnostic and therapeutic purposes [12]. The left coronary artery rises from the left sinus of Valsalva and courses laterally between the right ventricular outflow tract and left atrium. The optimized view for the left coronary ostium is similar to the coplanar view with slight leftward rotation (**Figure 4A**, **Table 2**). The right coronary artery rises from the right sinus of Valsalva and courses along the right atrioventricular groove laterally and caudally. The origin of the right coronary artery can sometimes locate more craniodorsally near, at, or above the STJ instead of the center of the right sinus [13]. The fluoroscopic view that keeps the right coronary ostium in plane resembles the cusp-overlapping view with a slight leftward rotation (**Figure 4B**, **Table 2**).

1.3.2 Optimized projections of the mitral valve

The mitral valve (MV) is likely the most studied cardiac valve in dogs due to the high prevalence of degenerative mitral valve disease in the species. The bifoliate MV consists of aortic (AL) and

parietal leaflets (PL) which cover two-thirds and one-third of the annular area respectively. The AL attaches to the aortomitral fibrous continuity and occupies one-third of the annular circumference between the medial and lateral fibrous trigones. In contrast, the other two thirds of the circumference is occupied by the hinge of the PL at the conjunction of atrial and ventricular myocardium [14]. According to the classic description of MV anatomy in the medical literature [15], the PL has two indentations at the free edge that divide the leaflet into three scallops identified as the P1, P2, and P3 segments in the lateral (left atrial appendage) to medial (interatrial septum) direction. The AL does not have clear indentations at the free edge but has three segments (A1, A2, A3) mirroring the three scallops on the PL (**Figure 5**).

When imaging the MV for interventional guidance, it is crucial to acquire fluoroscopic views that can visualize and localize all components of the MV including the annulus, leaflets, and subvalvular apparatus. The MV can be thoroughly examined via the standardized two-, three-, and four-chamber views of the left heart [1,16] similar to conventional echocardiographic imaging planes (**Figure 5**):

1.3.2.1 Two-chamber view (Intercommissural view)

The two-chamber view shows the overlapping AL and PL between the medial and lateral commissures. It is useful in orienting transcatheter devices in the medial-lateral direction along the zone of leaflet apposition. Other features of the two-chamber view include lateralization of the ostium of the left atrial appendage, separation of the left ventricular papillary muscles, and inspection of the mitral annulus in its major dimension (**Figure 5A**). This projection has a steep cranial angulation which may be impractical or hard to obtain (**Table 2**).

1.3.2.2 Three-chamber view (Inflow-outflow view)

The three-chamber view shows the left atrium, left ventricle, and aorta in a comparable orientation to the right parasternal inflow-outflow view on transthoracic echocardiography. It also gives the minor dimensions of the MV annulus in the aortoparietal direction (**Figure 5B**). In contrast to the two-chamber view, the AL and PL are fully separated with their scallops overlapped in the three-chamber view. This is an optimal projection for transcatheter mitral valve implantation due to its ability to visualize the full length of the left ventricular outflow tract and two partially overlapped papillary muscles at the caudolateral walls of the left ventricle. This projection has a mild caudal angulation with almost right lateral rotation in healthy dogs (**Table 2**).

1.3.2.3 Four-chamber view

The four-chamber view illustrates the spatial relationship between the four cardiac chambers (**Figure 5C**). Separation of the MV and tricuspid valves and visualization of the interatrial septum (IAS) may have value in guiding certain TCIs such as transeptal puncture, but the steep cranial angulation for this projection makes it difficult to obtain (**Table 2**).

1.3.3 Optimized projection of the pulmonary valve

Pulmonary valve (PV) interventions, such as balloon pulmonary valvuloplasty or transpulmonary stent implantation, are among the most performed TCIs in dogs. The anatomy of the PV resembles the AV except for the absence of coronary ostia. As described for the AV, the annulus of the PV is virtual as the ventriculoarterial junction is crown-like, not circular or ring-like. The three leaflets of the PV and their valvar sinuses are recognized as intermediate (non-adjacent to the aortic valve), left (mirroring the left aortic leaflet), and right (mirroring the right aortic leaflet) cusps. Two OFPs are defined for the PV (**Figure 6**).

1.3.3.1 Cusp overlap view

In comparison to the cusp-overlapping view of the AV, this projection of the PV isolates the left cusp (caudally positioned) with overlap of the intermediate and right cusps (cranially positioned). As a result, the PV appears in a bicuspid configuration with the virtual annulus extending from the nadir of the left pulmonary cusp to the base of the interleaflet triangle between the intermediate and right pulmonary cusps (**Figure 6A**). The minimal angulation of this view makes it easily achievable and useful for intra-operative guidance (**Table 2**).

1.3.3.2 Coplanar view

In the coplanar view, the nadirs of the intermediate, right, and left PV cusps are aligned to form the virtual annulus in plane. The intermediate and left cusps are separated to the side with central positioning of the right cusp. With this conformation of the PV cusps, the operator can quickly locate the annular plane and use it as a reference to deliver transcatheter devices (**Figure 6B**). However, the steep cranial angulation required may be difficult to achieve (**Table 2**).

1.3.4 Optimized projection of the interatrial septum

Transcatheter closure of interatrial shunts has been sporadically reported in veterinary cardiology [17–22]. On the other hand, atrial septostomy and left atrial decompression have emerged as a palliative intervention in dogs with advanced degenerative mitral valve disease [23]. While the use of transesophageal echocardiography has been well-described in performing atrial septostomy [24], simultaneous use of fluoroscopy can provide additional visualization of the transseptal puncture needle along its entire course and in relation to the IAS and surrounding structures. Three projections of the IAS were identified to have potential value in interventional guidance: The four-chamber view (as described in the mitral valve section, **Figure 5C** and **7B**), bicaval view, and short axis view of the IAS (**Figure 2** and **7**, **Table 2**).

1.3.4.1 Bicaval view

The bicaval view shows both the cranial and caudal caval veins and their entrance into the right atrium while keeping the oval fossa in-plane (**Figure 7A**). In dogs, the IAS locates immediately cranial to the entrance of the caudal caval vein and caudal to the intervenous tubercle and aortic root. The bicaval view is therefore useful in guiding the puncture in the cranial-caudal direction and to show the cranial and caudal rims of a secundum atrial septal defect if present. This projection has a moderate leftward rotation with mild caudal angulation (**Figure 2D** and **Table 2**).

1.3.4.2 Short axis view of the interatrial septum

The short axis view has the ability to visualize the aortic borders of the IAS and avoid aortic puncture during transseptal punction (**Figure 7C**). The amount of tissue at the aortic rim is associated with device selection, implant stability, and risk of complication in transcatheter closure of secundum atrial septal defects. Despite the potential value in fluoroscopic guidance, the almost vertical cranial angulation likely results in a projection that is impossible to achieve due to the physical constraints of the C-arm (**Figure 2D** and **Table 2**).

1.3.5 Effect of thoracic conformation on optimized fluoroscopic projections

The mean TD:TW of the nine dogs in the narrow chest group was higher than the nine dogs in the wide chest group ($p < 0.0001$; **Table 1**). All mean OFPs for each structure were compared and none were different between the two thoracic conformations (**Table 3**).

1.4 Discussion

The current study represents a proof of concept that determining structure-specific fluoroscopic projections of the canine heart is technically feasible. The need to optimize fluoroscopic projections began after the advent of transcatheter valve replacement therapy in

people, where the interventionalist relies heavily on the guiding fluoroscopic projection to accurately position and implant transcatheter devices in the heart [3,25,26]. Optimization of the guiding fluoroscopic views now plays a major role in the success of TCI and has become standard of care in people [3,6,7]. In contrast, there has only been one canine case report of transcatheter pulmonary valve implantation in the veterinary literature [27,28]. Nevertheless, detailed characterization of fluoroscopic and CCT cardiac anatomy is still valuable to the current and future practice of TCI in dogs.

The aortic, mitral, and pulmonary valves along with the interatrial septum were selected as SOI for this study based on their potential for future structural heart intervention development in dogs. The tricuspid valve was not included due to the relatively low prevalence of congenital malformations and unknown prognostic significance of acquired tricuspid valve diseases. Tricuspid valve interventions may become more relevant in the future if early correction of mitral regurgitation becomes more accessible, and the average lifespan of dogs prolongs. Surgical intervention under cardiopulmonary bypass is likely favored over transcatheter therapy for congenital tricuspid valve malformations due to anatomic considerations [29–32].

Instead of viewing the heart through the standard axial, coronal, and sagittal reconstructions of CT, the use of double-oblique MPR enables the observer to create any CCT imaging plane regardless of patient position. With this feature, one can identify the central axis (*en face* plane) for the SOI and predict intra-procedural C-arm coordinates to obtain the same image on fluoroscopy. Among the infinite number of views/projections orthogonal to this central axis, many of the selected OFPs resemble the standard echocardiographic views. This is not surprising as standardized echocardiographic views developed to highlight relevant anatomic detail as is proposed by the OFPs described in this study. Consistency in imaging planes and terminology is

advisable as it creates a modality-independent description of cardiac anatomy using attitudinally correct terms so that veterinary professionals can speak a common language [16]. As an example, when performing TCI at either the MV or left ventricular outflow tract, the same 3-chamber view of the left heart (**Figure 5B**) displayed on fluoroscopy and transesophageal echocardiography makes it much easier for the primary operator to grasp anatomic information and communicate with the rest of the procedural team.

The S curves play a major role in understanding fluoroscopic cardiac anatomy (**Figure 2**). Analysis of the S curve at either a disease population or individual level prior to intervention can help the clinician understand how to obtain optimal guiding fluoroscopic views for a patient going into the procedure [1,2,4,6,7]. In three dimensions, the S curves are arches of infinite projections perpendicular to the *en face* plane (line of perpendicularity). By studying the pattern of the S curves, particularly if available for a given disease state, one may estimate how to position the C-arm for certain structures without having a patient-specific CCT. For instance, the 3-chamber view of the mitral valve is very similar to either the standard right lateral fluoroscopic view with mild caudal angulation or left lateral view with mild cranial angulation (**Figure 2** and **Table 2**).

The c-arm coordinates reported in this study were generated assuming dorsal recumbency (the default of most medical imaging software in human). As many veterinary TCIs are performed in left or right lateral recumbencies, the coordinates will have to be transposed 90 degrees left- or rightward depending on the laterality of the patient. For example, the 3-chamber view of the mitral valve can likely be acquired in right lateral recumbency with zero rotation and a 20-degree cranial angulation of the C-arm. In cases where the transposed coordinate falls "under the fluoroscopic table" (with rotation and/or angulation angles greater than 90 degrees), one can likely go to the

opposite side of the c-arm by transposing LAO/RAO rotation by 180 degrees and mirror CRA/CAU angulation.

The comparison between the two thoracic conformations did not show a significant difference in any of the projections (**Table 3**). This is potentially positive, suggesting that the S curves and proposed OFP coordinates described here may be broadly applicable across dog morphotype. However, the dogs were divided into only two small groups which reduced the statistical power to detect such difference. The study also excludes brachycephalic breeds (anecdotally described as the barrel chest dogs) for concerns of lack of airway control during sedation. Previous studies measuring heart size on thoracic radiographs used arbitrary cut-offs of the TD:TW ratio to define thoracic conformation with the deep thorax group greater than 1.25, intermediate group between 0.75 and 1.25, and the broad thorax group as less than 0.75 [8,9]. Those cut-offs were not applied to this sample as almost all dogs would have been designated an intermediate conformation. Interestingly, we found that even in breeds that are traditionally considered to have deep or broad chests, their thoracic depth to width ratio was not as skewed as anticipated. Although we failed to demonstrate the effects of thoracic conformation on fluoroscopic projections, future studies including a broader breed composition and a larger sample size would be needed to confirm this finding.

The study has several few limitations. First, it has a small sample size which is inherent to the exploratory nature of the project. An *a priori* power analysis was deemed challenging due to the lack of pre-existing research data in dogs. Second, some of the OFPs in the study are difficult or almost impossible to obtain with conventional fluoroscopic equipment. The C-arm cannot be angulated from CRA 90 to CAU 90 due to its physical profile. In our experience, any cranial or caudal angulation exceeding 20 degrees is difficult to achieve because the C-arm will run into the

fluoroscopic table or the patient. Last, the results of this study are acquired from a very small group of apparently healthy dogs, which likely do not represent dogs with cardiovascular diseases that warrant intervention because of chamber remodeling and distorted anatomy.

1.5 Conclusion

The study has demonstrated the feasibility of optimizing fluoroscopic projections for individual canine cardiac structures utilizing CCT. Modality-independent imaging is not only valuable in guiding TCIs but also helpful in correlating imaging findings between different modalities and communications between clinicians. Thoracic conformation does not appear to have a significant effect on OFPs in apparently healthy dogs.

TABLES AND FIGURES – CHAPTER 1

Table 1.1: Summary of the study groups. The dogs were divided equally into wide chest and narrow chest groups based on their thoracic depth-to-width ratio. There are no differences in age or body weight between the two groups. The thoracic depth-to-width ratio is higher in the narrow chest group. FS, female spayed; MC, male castrated; TD, thoracic depth; TW, thoracic width.

	All dogs (n=18)	Wide chest (n=9)	Narrow chest (n=9)	*p* value
Age (years)	3.5 (1-10)	3.833 (1-10)	3.167 (1-5)	0.561
Sex	7 MC; 11 FS	6 MC; 3 FS	1 MC; 8 FS	
Body weight (kg)	23.16 (8.12-33)	22.38 (8.12-34)	24 (14.6-33)	0.661
Mean TD:TW	0.871	0.807	0.934	<0.0001
Breed	Ten mixed breed, two Staffordshire Bull Terrier, two Labrador Retriever, one Golden Retriever, one Cardigan Welsh Corgi, one Doberman Pinscher, one Italian Greyhound			

Table 1.2: Summary of optimal fluoroscopic projections (in degrees) from 18 apparently healthy dogs. The mean and 95% confidence cones (CC) are reported for each projection. CAU, caudal; CRA, cranial; LAO, left anterior oblique; RAO, right anterior oblique.

Aortic valve	*En face*			Coplanar			Cusp overlap			Left coronary			Right coronary		
	Mean	LAO 52	CAU 73	Mean	RAO 1	CRA 8	Mean	LAO 90	CRA 13	Mean	LAO 14	CRA 11	Mean	RAO 78	CAU 12
	95% CC	LAO 35-69	CAU 68-78	95% CC	RAO 8-LAO 6	CRA 1-15	95% CC	LAO 84-97	CRA 7-19	95% CC	LAO 7-21	CRA 4-18	95% CC	RAO 69-87	CAU 3-20
Mitral valve	*En face*			Two Chamber			Three Chamber			Four Chamber					
	Mean	LAO 16	CAU 32	Mean	RAO 25	CRA 49	Mean	RAO 89	CAU 21	Mean	LAO 26	CRA 57			
	95% CC	LAO 10-21	CAU 27-37	95% CC	RAO 20-31	CRA 45-53	95% CC	RAO 85-93	CAU 17-25	95% CC	LAO 21-31	CRA 54-60			
Pulmonary valve	*En face*			Coplanar			Cusp overlap								
	Mean	RAO 7	CAU 14	Mean	RAO 87	CRA 38	Mean	LAO 85	CAU 4						
	95% CC	RAO 15-LAO 1	CAU 7-21	95% CC	RAO 79-96	CRA 31-44	95% CC	LAO 78-91	CAU11 -CRA 2						
Interatrial septum	*En face*			Bicaval			Short axis			Four Chamber					
	Mean	RAO 55	CAU 21	Mean	LAO 41	CAU 12	Mean	RAO 89	CRA 64	Mean	LAO 7	CRA 51			
	95% CC	RAO 48-61	CAU 15-27	95% CC	LAO 35-48	CAU 6-18	95% CC	RAO 80-103	CRA 59-69	95% CC	LAO 1-13	CRA 47-55			

Table 1.3: Comparison of mean projections across all optimal fluoroscopic projections (in degrees) between dogs with narrow or wide chests. CAU, caudal; CRA, cranial; LAO, left anterior oblique; RAO, right anterior oblique.

Aortic valve	*En face*			Coplanar			Cusp overlap			Left coronary			Right coronary		
	Narrow	LAO 56	CAU 73	Narrow	RAO 3	CRA 9	Narrow	LAO 90	CRA 17	Narrow	LAO 13	CRA 11	Narrow	RAO 85	CAU 14
	Wide	LAO 47	CAU 74	Wide	LAO 1	CRA 8	Wide	LAO 92	CRA 10	Wide	LAO 14	CRA 10	Wide	RAO 72	CAU 9
	p value	0.3136		p value	0.7429		p value	0.0913		p value	0.7675		p value	0.0705	
Mitral valve0	*En face*			Two Chamber			Three Chamber			Four Chamber					
	Narrow	LAO 15	CAU 32	Narrow	RAO 27	CRA 49	Narrow	RAO 90	CAU 22	Narrow	LAO 25	CRA 57			
	Wide	LAO 16	CAU 32	Wide	RAO 24	CRA 50	Wide	RAO 88	CAU 21	Wide	LAO 27	CRA 57			
	p value	0.9989		p value	0.6014		p value	0.8769		p value	0.8726				
Pulmonary valve	*En face*			Coplanar			Cusp overlap								
	Narrow	RAO 9	CAU 12	Narrow	RAO 92	CRA 35	Narrow	LAO 79	CRA 0						
	Wide	RAO 5	CAU 16	Wide	RAO 82	CRA 40	Wide	LAO 98	CAU 9						
	p value	0.6707		p value	0.6268		p value	0.0619							
Interatrial septum	*En face*			Bicaval			Short axis			Four Chamber					
	Narrow	RAO 51	CAU 19	Narrow	LAO 47	CAU 12	Narrow	LAO 97	CAU 65	Narrow	LAO 13	CRA 53			
	Wide	RAO 59	CAU 23	Wide	LAO 36	CAU 11	Wide	LAO 87	CAU 62	Wide	LAO 2	CRA 49			
	p value	0.3416		p value	0.5130		p value	0.5395		p value	0.1142				

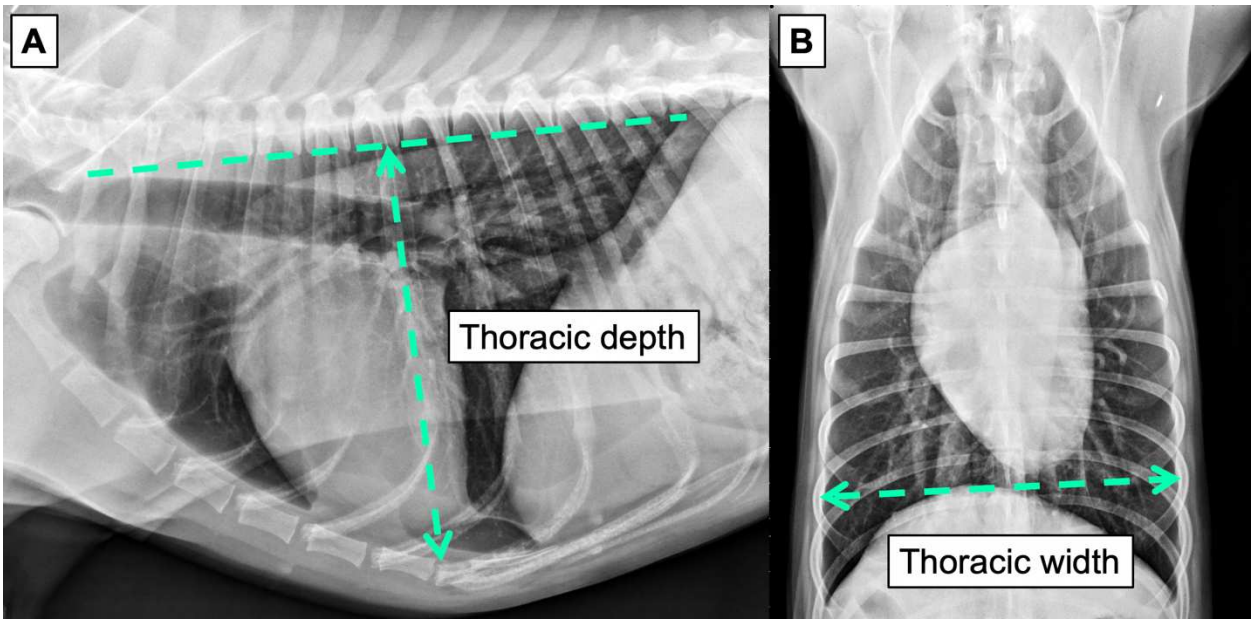

Figure 1.1: (A) Thoracic depth (dashed double arrow) as measured on the right lateral radiograph from the cranial edge of the xiphoid process to the ventral border of the vertebral column. (B) Thoracic width (dashed double arrow) as measured on the ventrodorsal radiograph as the linear dimension between the medial borders of the eighth ribs at their most lateral curvatures.

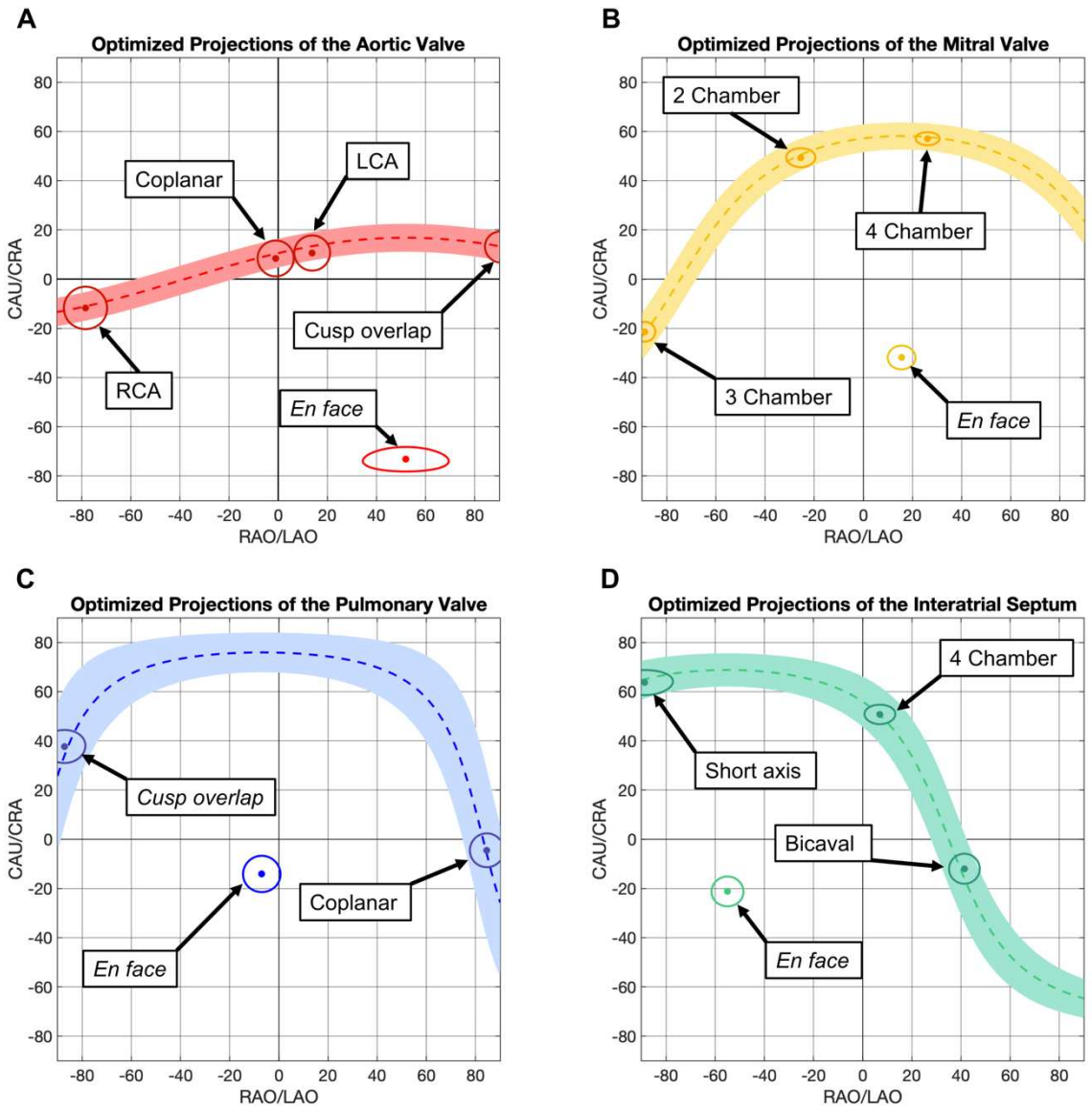

Figure 1.2: Optimized fluoroscopic projections (OFP) and S curves of the aortic valve (A), mitral valve (B), pulmonary valve (C), and interatrial septum (D). The mean (circular markers) and cone of 95% confidence (solid circle/ellipse) of the *en face* and individual OFPs are plotted and labeled. The figure also shows the mean (dashed curve) and 95% confidence (curved area) of the S curves for each structure. CAU, caudal; CRA, cranial; LAO, left anterior oblique; LCA, left coronary artery; RAO, right anterior oblique; RCA, right coronary artery.

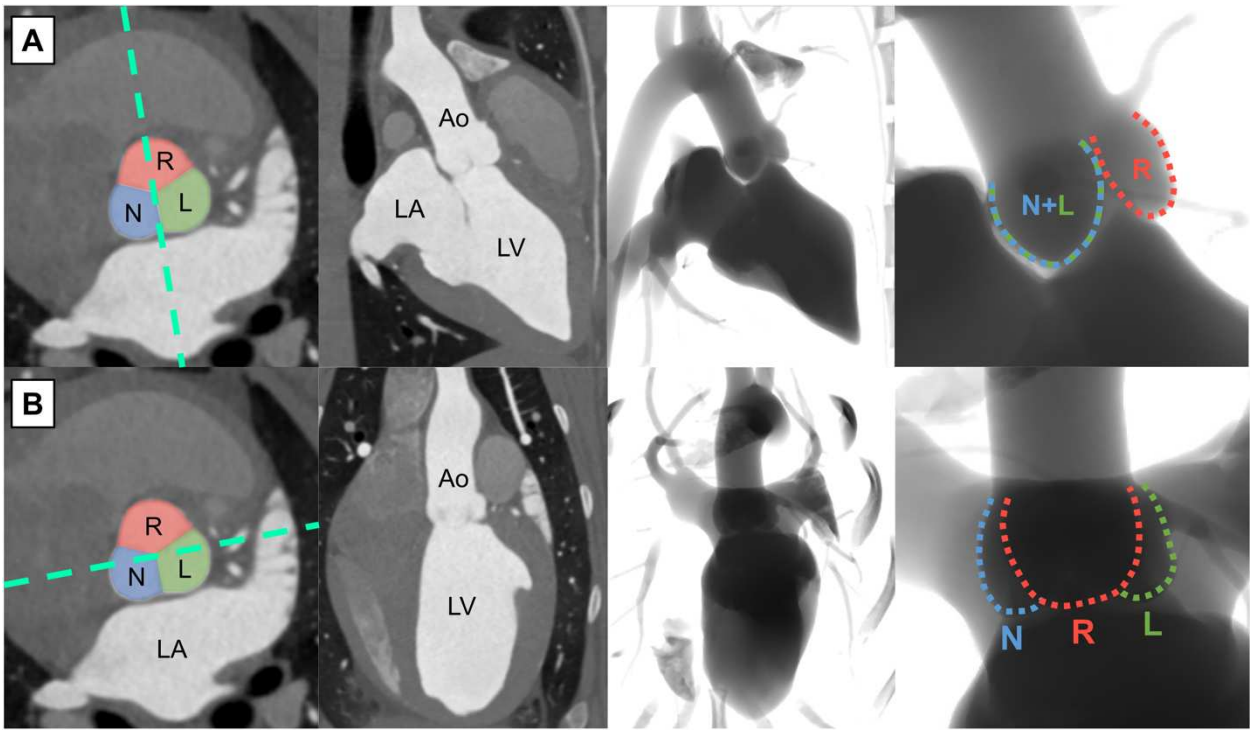

Figure 1.3: Optimized fluoroscopic projections of the aortic valve. Panel A: Multiplanar reformatting (MPR) image of the *en face* plane on the left with annotations of the right (red), left (green), and non-coronary (blue) cusps. The imaging plane for the cusp overlap view (turquoise dashed line) is also marked. The MPR and fluoroscopic images of the cusp overlap view show isolation of the right cusp (red dashed curve) and overlapping of the left (green dash curve) and non-coronary (blue dashed curve) cusps. Panel B: The coplanar view (turquoise dashed line) is shown on the *en face* MPR image. The MPR and fluoroscopic images of the coplanar view show central positioning of the right cusp (red dash curve) with all three cusps forming a straight line as the virtual annulus. Ao: aorta; LA: left atrium; LV: left ventricle.

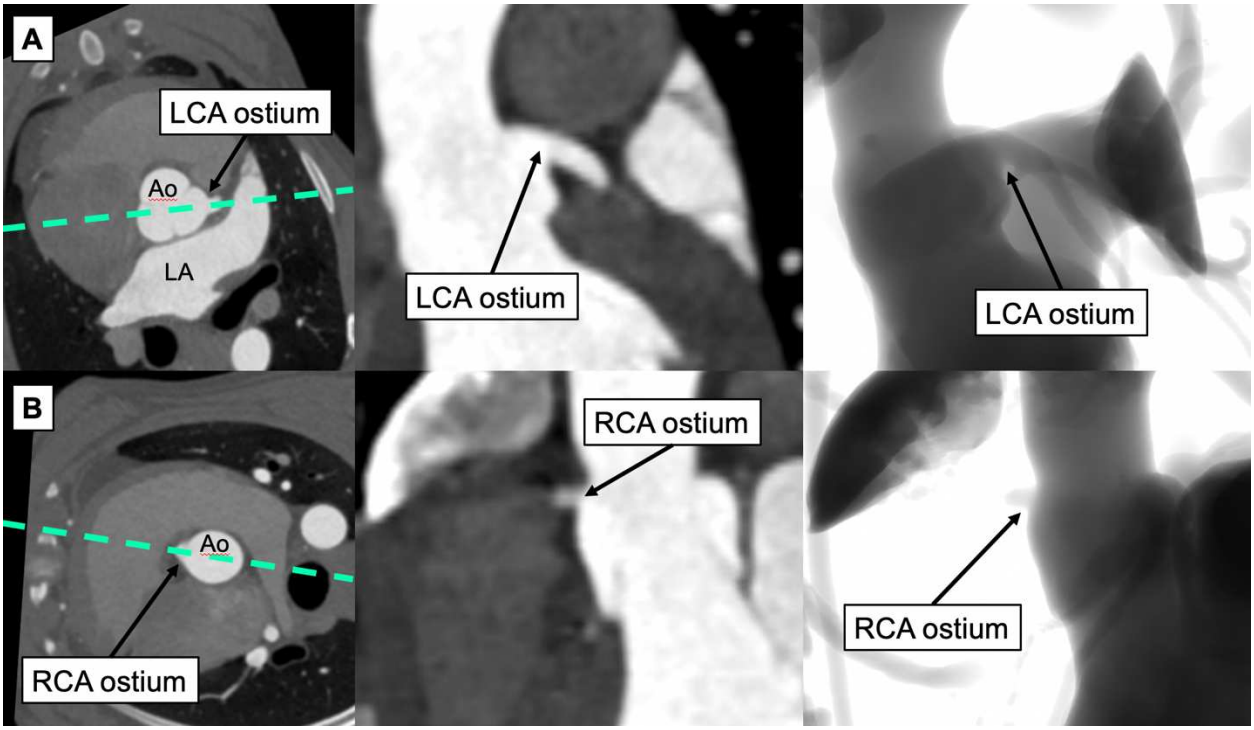

Figure 1.4: Multiplanar reformatting (MPR) and fluoroscopic images of the coronary ostia. Panel A: A MPR image of the aortic root. The imaging plane that best visualizes the left coronary ostium (turquoise dash line) is marked. The MPR and fluoroscopic images of the projection show a lateralized left coronary ostium and highlight the left main coronary artery. Panel B: Right coronary artery view (turquoise dash line) is marked on the MPR image of the sinotubular junction. The MPR and fluoroscopic images of the right coronary artery view highlight the right coronary ostia. Ao: aorta; LA: left atrium; LCA: left coronary artery; RCA: right coronary artery.

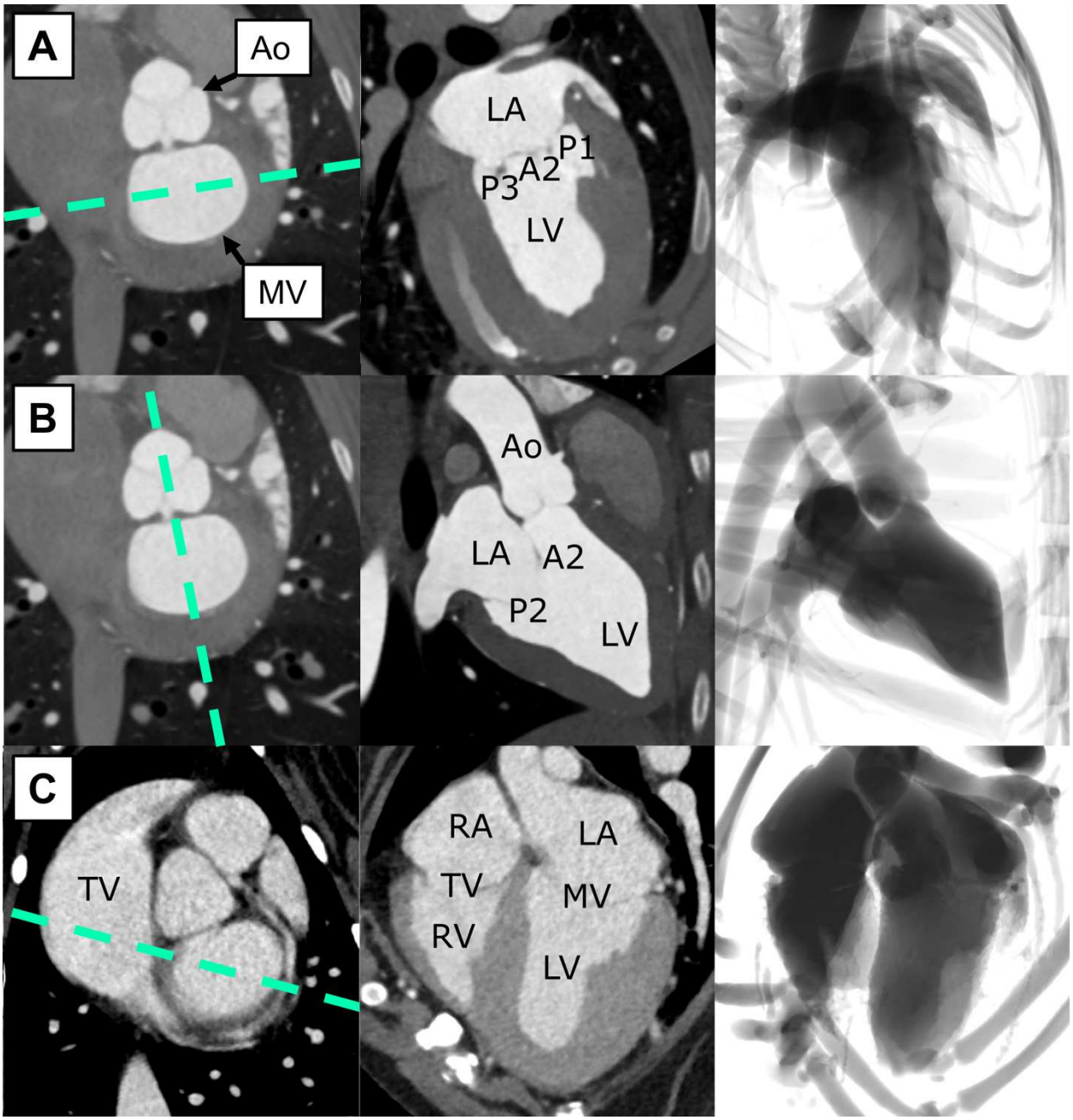

Figure 1.5: Optimal fluoroscopic projections of the mitral valve. Panel A: Multiplanar reformatting (MPR) of the MV *en face*, two-chamber, and fluoroscopic two-chamber views showing the imaging plane bisecting the mitral valve along the major axis (turquoise dashed line). The two-chamber view is considered equivalent to the intercommissural view of the MV on echocardiography. Panel B: The three-chamber view shows separation of the aortic and parietal leaflets but overlapping of the scallops (A1, A2, A3 and P1, P2, P3). The papillary muscles are overlapped. This view also shows the minor axis of the MV annulus. Panel C: Four chamber view of the MV resembling a right parasternal long axis four chamber view on echocardiography. Ao: aorta; LA: left atrium; LV: left ventricle; MV: mitral valve; RA: right atrium; RV: right ventricle; TV: tricuspid valve.

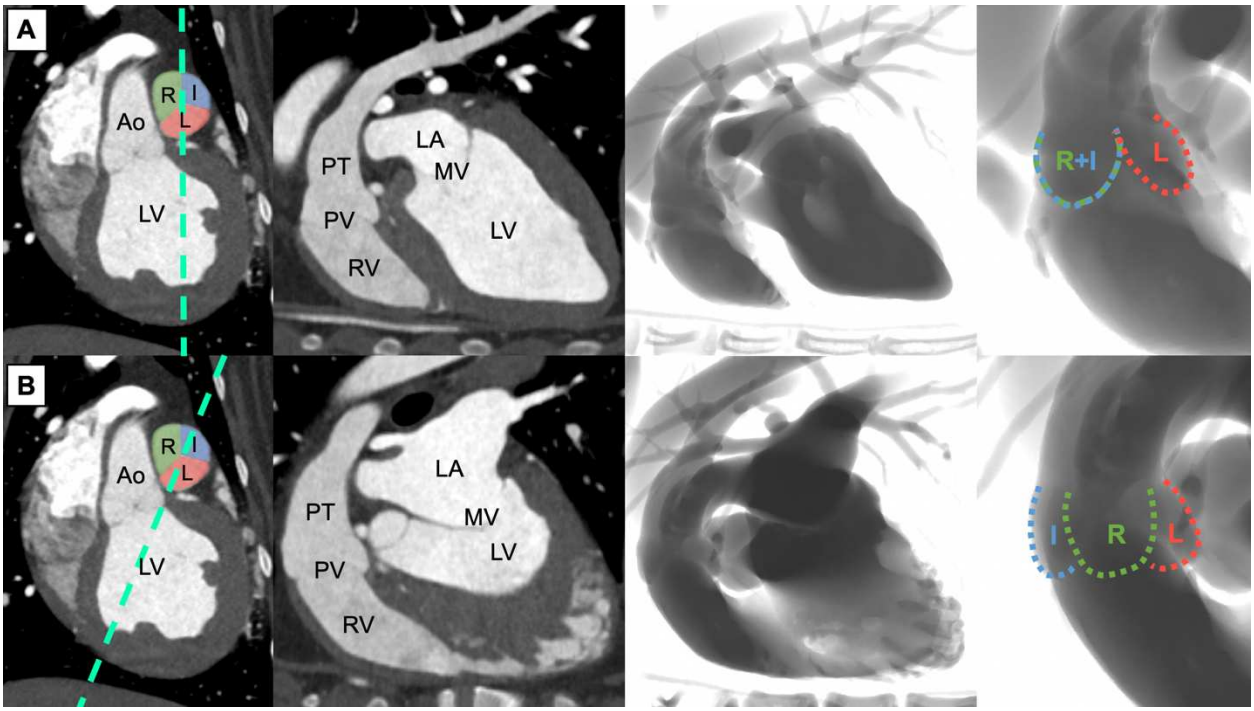

Figure 1.6: Pulmonary valve optimal fluoroscopic projections. The intermediate (blue), left (red), and right (green) pulmonary cusps are shown on the multiplanar reformatting *en face* view of the pulmonary valve (PV). Panel A shows the cusp overlap view (turquoise dashed line) where the right (green) and intermediate (blue) cusps are overlapped with isolation of the left (red) cusp. Panel B shows the pulmonary cusp overlap view where the right (green) cusp is in the center with the hinges of all three cusps on the same plane resulting in definition of the virtual annulus. Ao: aorta; LA: left atrium; LV: left ventricle; MV: mitral valve; PT: pulmonary trunk; RV: right ventricle.

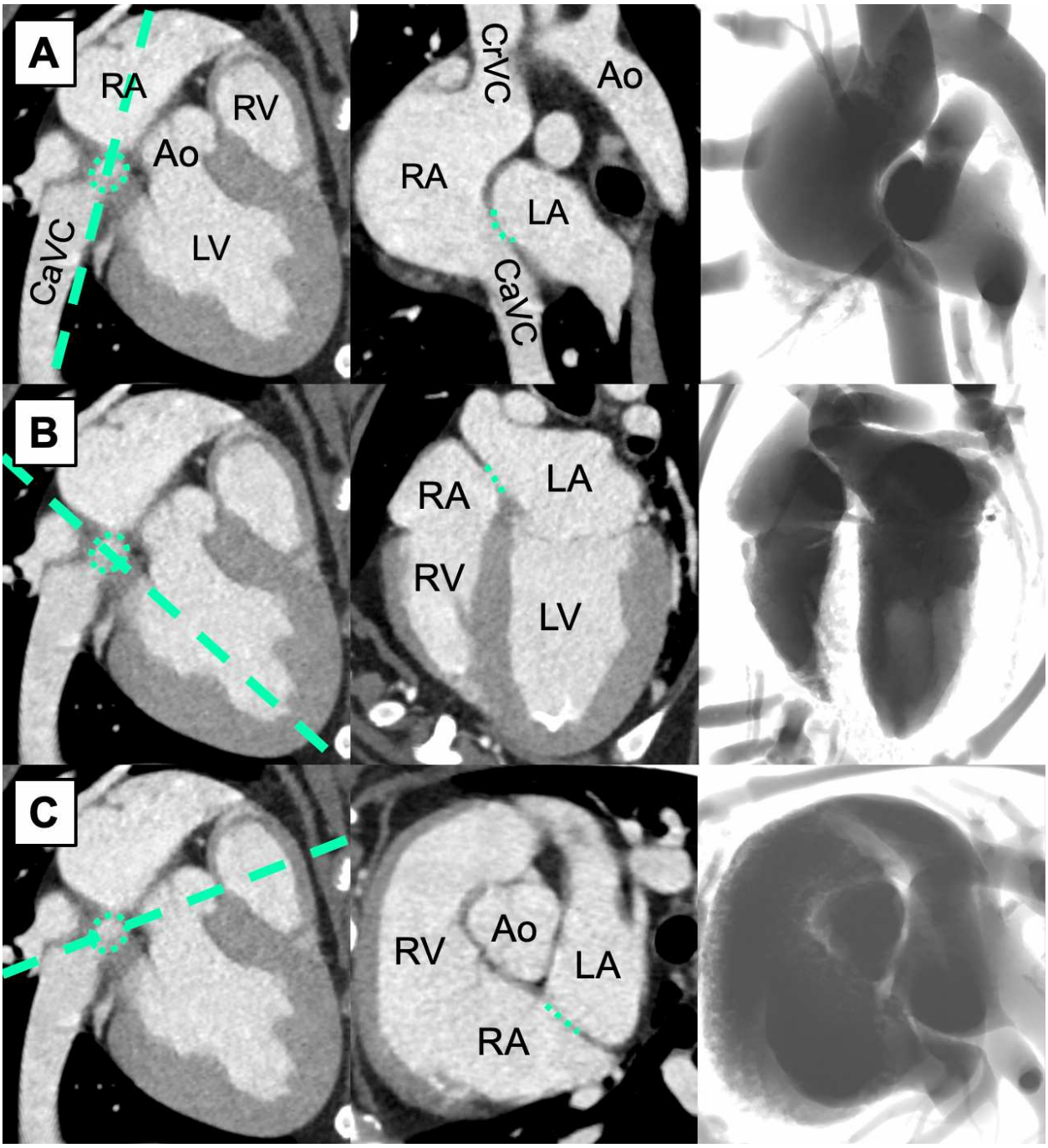

Figure 1.7: Optimal fluoroscopic projections of the interatrial septum (IAS). The *en face* view of IAS (turquoise dash circle) is shown on the left of each panel with corresponding imaging planes (turquoise dash lines). Panel A: Bicaval view visualizing both the cranial and caudal caval veins with the IAS (turquoise dash curve) shown cranial to the caudal cavoatrial junction. Panel B: Four-chamber view of the left heart with the IAS in-plane. Panel C: Short axis view of the IAS where the aortic border of the IAS (turquoise dash curve) can be visualized. Ao: aorta; CaVC: caudal vena cava; CrVC: cranial vena cava; LA: left atrium; LV: left ventricle; RA: right atrium; RV: right ventricle.

REFERENCES - CHAPTER 1

[1] Thériault-Lauzier P, Andalib A, Martucci G, Mylotte D, Cecere R, Lange R, Tchétché D, Modine T, Van Mieghem N, Windecker S, Buithieu J, Piazza N. Fluoroscopic anatomy of left-sided heart structures for transcatheter interventions. JACC: Cardiovascular Interventions 2014;7:947–57.

[2] Pighi M, Thériault-Lauzier P, Alosaimi H, Spaziano M, Martucci G, Xiong T-Y, Buithieu J, Ybarra LF, Afilalo J, Leipsic J, Ozden Tok O, Mousavi N, Mangiameli A, Pilgrim T, Praz F, Windecker S, Piazza N. Fluoroscopic anatomy of right-sided heart structures for transcatheter interventions. JACC: Cardiovascular Interventions 2018;11:1614–25.

[3] Leipsic J, Gurvitch R, LaBounty TM, Min JK, Wood D, Johnson M, Ajlan AM, Wijesinghe N, Webb JG. Multidetector computed tomography in transcatheter aortic valve implantation. JACC: Cardiovascular Imaging 2011;4:416–29.

[4] Spaziano M, Thériault-Lauzier P, Meti N, Vaquerizo B, Blanke P, Deli-Hussein J, Chetrit M, Galatas C, Buithieu J, Lange R, Martucci G, Leipsic J, Piazza N. Optimal fluoroscopic viewing angles of left-sided heart structures in patients with aortic stenosis and mitral regurgitation based on multislice computed tomography. Journal of Cardiovascular Computed Tomography 2016;10:162–72.

[5] Pontone G, Rossi A, Guglielmo M, Dweck MR, Gaemperli O, Nieman K, Pugliese F, Maurovich-Horvat P, Gimelli A, Cosyns B, Achenbach S. Clinical applications of cardiac computed tomography: a consensus paper of the European Association of Cardiovascular Imaging-part II. Eur Heart J Cardiovasc Imaging 2022;23:e136–61.

[6] Zgheib A, Campens L, Abualsaud A, Al Isma'ili A, Barbanti M, Dvir D, Gada H, Granada JF, Latib A, Leipsic J, Maisano F, Martucci G, Medina De Chazal HA, Modine T, Mylotte D, Prendergast B, Sawaya F, Spaziano M, Tang G, Theriault-Lauzier P, Tchetche D, Van Mieghem N, Søndergaard L, De Backer O, Piazza N. Aortic annulus s-curve. JACC: Cardiovascular Interventions 2022;15:2353–73.

[7] Blanke P, Weir-McCall JR, Achenbach S, Delgado V, Hausleiter J, Jilaihawi H, Marwan M, Norgaard BL, Piazza N. Computed tomography imaging in the context of transcatheter aortic valve implantation (TAVI) / transcatheter aortic valve replacement (TAVR): An expert consensus document of the Society of Cardiovascular Computed Tomography. Journal of Cardiovascular Computed Tomography 2019;13:1–20.

[8] Buchanan JW, Bücheler J. Vertebral scale system to measure canine heart size in radiographs. J Am Vet Med Assoc 1995;206:194–9.

[9] Bodh D, Hoque M, Saxena AC, Gugjoo MB, Bist D, Chaudhary JK. Vertebral scale system to measure heart size in thoracic radiographs of Indian Spitz, Labrador retriever and Mongrel dogs. Vet World 2016;9:371–6.

[10] Sá JPM de. Applied statistics: using SPSS, Statistica, MATLAB, and R. 2nd ed. Berlin ; New York: Springer; 2007.

[11] Tretter JT, Spicer DE, Jacobs JP, Anderson RH. The aortic valve with two leaflets. JTCVS Open 2022;9:89–90.

[12] Meurs KM, Lehmkuhl LB, Bonagura JD. Survival times in dogs with severe subvalvular aortic stenosis treated with balloon valvuloplasty or atenolol. J Am Vet Med Assoc 2005;227:420–4.

[13] Scansen BA. Coronary artery anomalies in animals. Vet Sci 2017;4:20.

[14] Barszcz K, Goździewska-Harłajczuk K, Czopowicz M, Chłopecka M, Polguj M, Klećkowska-Nawrot J. Morphometry and topography of the coronary ostia in the dog. J Vet Res 2023;67:471–8.

[15] Fox PR. Pathology of myxomatous mitral valve disease in the dog. Journal of Veterinary Cardiology 2012;14:103–26.

[16] Carpentier AF, Lessana A, Relland JYM, Belli E, Mihaileanu S, Berrebi AJ, Palsky E, Loulmet DF. The "Physio-Ring": an advanced concept in mitral valve annuloplasty. The Annals of Thoracic Surgery 1995;60:1177–86.

[17] Piazza N, Mylotte D, Theriault Lauzier P. Fluoroscopic "heart chamber" anatomy – the case for imaging modality-independent terminology. EuroIntervention 2016;12:Y9–15.

[18] Gordon SG, Miller MW, Roland RM, Saunders AB, Achen SE, Drourr LT, Nelson DA. Transcatheter atrial septal defect closure with the Amplatzer atrial septal occluder in 13 dogs: short- and mid-term outcome. J Vet Intern Med 2009;23:995–1002.

[19] Gordon SG, Nelson DA, Achen SE, Miller MM, Roland RM, Saunders AB, Drourr LT. Open heart closure of an atrial septal defect by use of an atrial septal occluder in a dog. J Am Vet Med Assoc 2010;236:434–9.

[20] Shelden A, Wesselowski S, Gordon SG, Saunders AB. Transcatheter closure of a small atrial septal defect with an Amplatzer™ patent foramen ovale occluder in a working dog with cyanosis and exercise intolerance at high altitude. J Vet Cardiol 2017;19:523–9.

[21] Sanders RA, Hogan DF, Green HW, Hoyer MH, Puppel DA. Transcatheter closure of an atrial septal defect in a dog. Journal of the American Veterinary Medical Association 2005;227:430–4.

[22] Pelzek C, Rhinehart JD, Villalba M, Schober KE, Winter RL, Berman D. Transient high-grade second-degree atrioventricular block secondary to transvenous atrial septal defect occlusion in a dog. J Vet Cardiol 2022;41:30–8.

[23] Sugimoto K, Mochizuki Y, Kanda T, Ohnishi A, Miyabe M, Wada Y, Kochi M, Aoki T. Atrial septal defect closure in a midget toy poodle. Open Vet J 2020;10:11–5.

[24] Allen JW, Phipps KL, Llamas AA, Barrett KA. Left atrial decompression as a palliative minimally invasive treatment for congestive heart failure caused by myxomatous mitral valve disease in dogs: 17 cases (2018-2019). J Am Vet Med Assoc 2021;258:638–47.

[25] Allen J, Phipps K, Barrett K. Transseptal puncture in the dog utilizing three-dimensional transesophageal echocardiographic guidance. J Vet Cardiol 2024;51:64–71.

[26] Arnold M, Achenbach S, Pfeiffer I, Ensminger S, Marwan M, Einhaus F, Pflederer T, Ropers D, Schuhbaeck A, Anders K, Lell M, Uder M, Ludwig J, Weyand M, Daniel WG, Feyrer R. A method to determine suitable fluoroscopic projections for transcatheter aortic valve implantation by computed tomography. Journal of Cardiovascular Computed Tomography 2012;6:422–8.

[27] Binder RK, Leipsic J, Wood D, Moore T, Toggweiler S, Willson A, Gurvitch R, Freeman M, Webb JG. Prediction of optimal deployment projection for transcatheter aortic valve replacement: angiographic 3-dimensional reconstruction of the aortic root versus multidetector computed tomography. Circ: Cardiovascular Interventions 2012;5:247–52.

[28] Borenstein N, Chetboul V, Passavin P, Morlet A, Fernandez-Parra R, Carazo Arias LE, Giannettoni G, Saponaro V, Poissonnier C, Ghazal S, Lefort S, Trehiou-Sechi E, Marchal CR, Delle Cave J, Vannucci E, Behr L, Verwaerde P. Successful transcatheter pulmonary valve implantation in a dog: first clinical report. J Vet Cardiol 2019;26:10–8.

[29] Terrade G, Borenstein N, Chetboul V, Toma C, Guillaume E, Bruneval P, Fiette L, Carazo Arias LE, Morlet A, Le Dudal M. First reported long-term two- and three-dimensional echocardiographic follow-up with histopathological analysis of a transcatheter pulmonary valve implantation in a pet dog. J Vet Cardiol 2024;53:52–9.

[30] Arai S, Griffiths LG, Mama K, Hackett TB, Monnet E, Boon JA, Carter L, Orton EC. Bioprosthesis valve replacement in dogs with congenital tricuspid valve dysplasia: technique and outcome. J Vet Cardiol 2011;13:91–9.

[31] Sutherland BJ, Pierce KV, Heffner GG, Scansen BA, Miller MW, Grey P, Orton EC. Surgical repair for canine tricuspid valve dysplasia: Technique and case report. J Vet Cardiol 2021;33:34–42.

[32] Bristow P, Sargent J, Luis Fuentes V, Brockman D. Outcome of bioprosthetic valve replacement in dogs with tricuspid valve dysplasia. J Small Anim Pract 2017;58:205–10.

[33] Bristow P, Kurosawa A, Fuentes VL, Rutherford L, Brockman D. Surgical valvulotomy for tricuspid valve stenosis in a dog. J Vet Cardiol 2019;23:142–8.

CHAPTER 2: CHARACTERIZATION OF OPTIMIZED FLUOROSCOPIC PROJECTIONS OF THE PULMONARY VALVE IN DOGS WITH PULMONARY STENOSIS USING CARDIAC COMPUTED TOMOGRAPHY

2.1 Introduction

Transcatheter pulmonary valve interventions (TPVI) such as balloon pulmonary valvuloplasty or transpulmonary stent implantation are one of the most commonly performed cardiac interventions in dogs. Fluoroscopic guidance during these procedures is often defaulted to acquire a standard lateral projection of the thorax (typically with the animal in left lateral recumbency) and not an optimal perspective of the pulmonary valve (PV). Such practice can result in fluoroscopic parallax making it challenging for the interventionalist to recognize and measure anatomic landmarks of the PV such as the annulus. To resolve this issue, the X-ray beam should be positioned orthogonally to the central trajectory or *en face (facing the valve*) projection of the PV [1]. The resultant projections are defined as optimized fluoroscopic projections (OFP) that situate along an arch of infinite projections above the fluoroscopic table (optimal projection curve or S curve). Acquisition of OFPs for cardiac structures has proven to be feasible using cardiac computed tomography (CCT) in people [1–3]. The OFPs of the PV have not been characterized in dogs with pulmonary valve stenosis (PS).

Accurate sizing of the PV annulus is essential to the selection of transcatheter devices during TPVI. Cardiac CT provides precise measurements of the PV apparatus and can serve as a reference standard due to its high spatial resolution and ability to characterize cardiac anatomy in three dimensions. By using CCT as the clinical benchmark, the accuracy of transthoracic

echocardiography (TTE) and angiocardiography can be examined, investigating whether the more widely accessible imaging modalities provide results that are consistent with a reference method.

The objectives of this study were to 1) characterize the OFPs of the PV in dogs with severe PS, 2) compare the OFPs between apparently healthy dogs and dogs with severe PS, and 3) report the biases and agreements in measured PV annular diameter between CCT, TTE, and angiocardiography.

2.2 Material and method

2.2.1 Case selection

Dogs that were referred to Colorado State University Veterinary Teaching Hospital for severe PS (reported peak systolic transpulmonary pressure gradient on spectral Doppler echocardiography exceeding 80 mmHg) were retrospectively selected from the electronic medical record system. The dogs had to have undergone TTE, CCT, and angiocardiography for TPVI (balloon valvuloplasty or transpulmonary stent implantation) within the same week. All dogs had to have no other major congenital cardiac defects and the CCT study had to be of high quality (retrospective gating with full contrast opacification of the PV apparatus and without major artifacts). Cardiac CT studies from a group of apparently healthy dogs were used as a matched normal control for the comparison of OFPs. This group of healthy dogs had been previously enrolled in another research project investigating CCT.

2.2.2 Cardiac computed tomography – Image acquisition

A dual source, 384-slice (192 slices in each detector row) computed tomography scanner (SOMATOM Force Dual Source CT scanner, Siemens Medical Solutions, Malvern, PA, USA) with retrospective cardiac gating was used to acquire all CCTs. The CCTs of the PS group were

acquired with a standardized protocol for canine PS at the authors' institution: The dogs were anesthetized and positioned on the CT table in ventral recumbency. A pre-contrast thoracic CT was first acquired and reconstructed in order to select the monitoring slice for bolus tracking. A region of interest with a threshold of 150 Hounsfield units was placed in the pulmonary trunk to acquire the dextrophase and then the levophase after a delay of 6 to 8 seconds based on the heart rate. A triphasic contrast (Iohexol 300 mgI/mL, Omnipaque™, GE Healthcare, Chicago, IL, USA) protocol delivering a total of 1.5 mL/kg contrast was used: 1 mL/kg of 100% contrast at 1 to 3 ml/s, followed by 1 mL/kg of 50% contrast-to-saline mixture at 1 to 3 ml/s, and a final 1 mL/kg saline bolus at 1 to 3 ml/s. The contrast injection rate was variable according to the body weight of the patient while aiming for an injection time of 5 to 6 seconds for each phase of bolus. All studies were reconstructed at 0.75 mm slice thickness with the field-of-view containing the entire heart and great vessels. Both the levophase and dextrophase scans were reconstructed into 20 phases at 5% increments of the R-to-R cycle length and stored for further analysis.

The CCTs for PS dogs were acquired under general anesthesia and positive-pressure mechanical ventilation with 100% oxygen. A short burst of hyperventilation was given prior to imaging, and the patient was in a brief period of apnea during image acquisition. The CCT images of the normal group were acquired under brief sedation and spontaneous respiration. The sedatives were administered (butorphanol 0.2 to 0.4 mg/kg IV with titrated boluses of alfaxalone at 0.5 to 1 mg/kg IV) when the dog entered the CCT room and sedation was monitored by the Anesthesia and Pain Management Service at the authors' institution. Pulse rate, ECG, peripheral oxygen saturation, and oscillometric blood pressure were monitored during all CCTs.

2.2.3 Cardiac computed tomography – Imaging analyses

All CT images were analyzed with a proprietary CT software (Syngo.via Cardiac Function application, Siemens Medical Solutions USA, Malvern, PA, USA). The three PV leaflets and the nadir of the hinge points were first identified in double-oblique multiplanar reformatting. The PV annular plane containing all three nadirs was then defined as the *en face* (facing the valve) projection (**Figure 1A**). Two OFPs perpendicular to the *en face* were then derived: The cusp-overlap (CO) and coplanar (CP) views (**Figure 1B** and **1C**). The CO view results in overlap of the intermediate and right leaflets with isolation of the left leaflet. The annular plane is defined as the line connecting the left and right/intermediate hinge points. The CP view establishes the nadir of all three sinuses along the same plane with central positioning of the right sinus. The theoretical left/right anterior oblique (LAO/RAO) rotations and cranial/caudal (CRA/CAU) angulations of the corresponding views (in degrees) were autogenerated by the software assuming the dog is in dorsal recumbency.

For dogs in the PS group, the effective PV diameter ($PV_{Eff} = 2 \times \sqrt{\frac{PV\ Area}{\pi}}$) was derived as the theoretical diameter of the PV annulus that will give a circular area equivalent to the planimetered elliptical annular area on CCT. The linear PV annular diameter on the CO (PV_{CO}) and CP (PV_{CP}) views were also measured. To detect potential differences in body shape between the healthy and PS groups which may influence thoracic conformation and anatomic positioning of cardiac structures, the thoracic depth-to-width ratio (TDTWR) was acquired in all dogs and was used as an index of chest conformation (**Figure 2**). In short, thoracic depth was considered the distance between the cranial border of the xiphoid process and the ventral border of the vertebral column on the central sagittal plane. This linear measurement was perpendicular to a virtual line parallel to the vertebral column (**Figure 2A**). Thoracic width was measured on the transverse plane

as the linear dimension between the medial borders of the eighth ribs at their most lateral curvatures (**Figure 2B**). The TDTWR was then calculated as thoracic depth divided by the thoracic width.

2.2.4 Optimal projection curve (S curve) of the pulmonary valve

A trigonometric formula was used to describe the three-dimensional arch of infinite OFPs of the PV from CCT [3,4]:

$$\phi = -\arctan\frac{\cos(\theta - \theta_{en\ face})}{\tan\phi_{en\ face}}$$

Where the angulation ($\phi_{en\ face}$) and rotation ($\theta_{en\ face}$) of the *en face* projection are known, the CRA/CAU angulation (ϕ) of the OFP was determined by its LAO/RAO rotation (θ). This trigonometric relationship represents an infinite number of projections perpendicular to the *en face*, which can be plotted onto a geographic coordinate system (consider LAO/RAO rotation as the longitude and CRA/CAU angulation as the latitude) to generate the optimal projection curve (also known as S curve due to its s shape) of the PV (**Figure 3**). This assumes the dog was positioned in dorsal recumbency on the fluoroscopic table with the heart at the center of the coordinate system.

2.2.5 Transthoracic echocardiography

Selected transthoracic echocardiographic studies were retrospectively reviewed by a single observer (IBC) using an offline imaging software (Syngo® Dynamic Workplace, Siemens Medical Solutions, Inc., Malvern, PA, USA). The PV diameter (PV_{TTE}) was measured in early-to-mid systole between the hinge point of the leaflets on the right parasternal short axis view at the level of the PV and pulmonary trunk. The measurement was made in triplicate and the average diameter used for analysis.

2.2.6 Angiocardiography

The intra-operative right ventriculogram in a standard lateral projection from all dogs were retrospectively reviewed using an offline radiology software (IntelliSpace Radiology, Philips Healthcare Informatics, Inc., Andover, MA, USA). The pulmonary valve diameter (PV_{Angio}) was measured in early-to-mid systole between the hinge points of the opened leaflets. Three cardiac cycles were measured to derive the average diameter. All angiographic images were auto-calibrated by the fluoroscopic system (Allura Xper FD 20 with Clarity, Philips Healthcare, Andover, MA, USA) at the time of TPVI.

2.2.7 Statistics

All continuous variables are examined for normality using Shapiro-Wilk test. Student's t-test or Wilcoxon rank-sum test was used for parametric and non-parametric comparison of means/medians. Statistical methods described in directional statistics were used to analyze the C-arm rotation (LAO/RAO) and angulation (CRA/CAU) as geographical coordinates [5]. For each sample of spherical coordinates, von Mises-Fisher distribution was evaluated with visual inspection of longitude and colatitude plots. The mean S curves and 95% confidence curve areas of both the normal and PS groups were generated from the means and 95% cones of confidence of each PV *en face* coordinate. The 95% cone of confidence was calculated from the 95% deviation angle of each spherical coordinate sample. Mean *en face* and OFPs of the two groups were compared using the two-sample Watson-Williams test. Bland-Altman analyses were conducted to examine the agreements and biases between different measurements of the PV annulus made on CCT projections, TTE, and intra-procedure angiocardiography in lateral projection. Simple linear regression was used to detect proportional bias in the Bland-Altman statistics. The significance level (alpha) of the study was set at 0.05. Statistical analyses and graphics of the spherical statistics

were compiled using a proprietary programming language and computing environment (MATLAB R2024b, The MathWorks, Inc., Natick, MA, USA). The standard statistics including the Bland-Altman analyses were computed using an open-source programming language and software environment (R version 4.4.1 [Race for your life]; RStudio version 2024.09.0+375, Posit Software, Boston, MA, USA).

2.3 Results

2.3.1 Study group characteristics

Eighteen dogs were selected between September 2020 and February 2024. All dogs had isolated severe PS except for one dog with patent foramen ovale and another dog (14.8 kg in body weight) with a diminutive (2 mm) perimembranous ventricular septal defect. The dogs in the PS group were smaller in size ($p < 0.0001$) compared to the normal group but not significantly different in age or thoracic conformation. Most of the PS group were French bulldogs whereas no brachycephalic breeds were in the normal group. Sample characteristics of both the normal and PS groups are summarized in **Table 1**.

2.3.2 Comparing optimized fluoroscopic projections of the pulmonary valve

The mean *en face* projection of the PS group had more rightward rotation but was not significantly different from the normal group ($p = 0.104$, **Table 2** and **Figure 3**). The mean S curve of the PS group also have more rightward rotation compared to the normal group (**Figure 3**). The mean CO projections of both groups had mild CRA/CAU angulation with the PS group having less leftward rotation consistent with the S curves ($p = 0.017$, **Table 2** and **Figure 3**). The mean CP projections between the two groups were distant from each other ($p < 0.001$, **Table 2** and **Figure 3**).

2.3.3 Bland-Altman analyses on different pulmonary annular measurements

There was good agreement between the PV_{eff}, PV_{CO}, and PV_{CP} with no systemic bias and narrow limits of agreements (**Table 3**, **Figure 4A** and **4B**). However, TTE appeared to systemically underestimate PV annulus diameter with wide limits of agreement (**Table 3**, **Figure 4C**). There was also proportional bias as data values increased ($p < 0.001$). There was no systemic bias detected between PV_{eff} and PV_{Angio}. However, the limits of agreement were wider when compared to the agreements between CCT measurements (**Table 3** and **Figure 4D**) and there was proportional bias as data values increased ($p = 0.001$). Bland-Altman statistics are summarized in **Table 3**.

2.4 Discussion

The present study shows that dogs with severe PS have distinct and different patterns of S curves and OFPs of the PV compared to healthy dogs. Additionally, the standard lateral projection of the thorax (90 degrees LAO/RAO rotation with no CRA/CAU angulation) is suboptimal for TPVI and susceptible to fluoroscopic parallax of the PV and this potential parallax is exacerbated in the setting of severe PS. Optimization of the intra-procedural fluoroscopic projection ensures precise identification of anatomic landmarks (especially the annulus and valve hinge points) and has become standard of care during transcatheter valve replacement in people [4,6]. The optimized fluoroscopic views help the operator localize the annulus in-plane and use it as a reference to accurately position and deploy bioprosthetic valves. In contrast, stenting or bioprosthetic valve implantation are only considered in select dogs with more complicated form of congenital PS while balloon valvuloplasty remains the first-line intervention in most cases [7–14]. The same level of precision may not be required for balloon valvuloplasty as the procedure does not involve

permanent implants and repeated ballon dilation of the pulmonary valve is considered safe in most cases. Nonetheless, further understanding of PV fluoroscopic anatomy may facilitate optimal angiographic measurements and improve anatomic localization. The OFPs defined in this study may have utility when transcatheter valve replacement becomes viable in dogs [13].

Even though the OFPs and the S curve represent all 360 degrees around the *en face* projection, not all projections are practically obtainable on a traditional fluoroscopic table. From the authors' experience, a CRA or CAU angulation steeper than 20 degrees is hard to achieve due to the physical constraint of the C-arm (either the X-ray tube or the detector will interfere with the fluoroscopic table and patient). Use of CRA/CAU angulation will also limit the range of left/right rotation the C-arm can achieve. For this reason, the CO view appears to be an ideal projection for TPVI in canine PS since the CP projection has a steeper mean angulation. However, variability in inherent cardiac anatomy and severity of remodeling between dogs with PS must be considered and individualized OFPs based on patient specific CCT studies may be required. An insignificant difference in the *en face* location can have major impacts on the S curve and resultant OFPs (such as that seen between the two groups in this study).

Appropriate sizing of transcatheter devices relies on accurate measurement of the PV apparatus. Given the non-circular nature of the PV annulus, a single linear measurement from any perspective carries the potential to over- or underestimate the size of the annulus [15,16]. The results of the Bland-Altman analyses showed good agreement between the PV_{CO}, PV_{CP}, and PV_{Eff} diameters suggesting that the diameters measured on the OFPs should give a close estimation of the true pulmonary annulus. On the other hand, PV_{TTE} significantly underestimated PV annular size and had low agreement with the PV_{Eff}. Transthoracic echocardiography is the first-line diagnostic test for congenital PS and is used for preliminary sizing of the PV in dogs. This Bland-

Altman analysis between TTE and CCT should alert clinicians that the PV diameter measured on TTE may be unreliable and not represent the true size of the PV annulus. There was no systemic bias between the PV_{Eff} and PV_{Angio}, but the wider limits of agreement and proportional bias within the data range argue that PV annular measurements made by CCT are more precise (and potentially more accurate) than the angiographic measurement from a standard lateral projection of the thorax. When selecting balloon dilation catheters for balloon valvuloplasty, a 30 to 50% oversizing to the annular diameter is often chosen but this degree of oversizing is not guided by prospective veterinary studies. Other factors such as operator experience, limitations in inventory, or mechanism and severity of PS (e.g., a larger balloon catheter with higher rated burst pressure may be chosen for severe, dysplastic stenosis to generate higher radial force) also affect the decision-making process. For the above reasons, selection of balloon dilation catheters can be arbitrary, imprecise, and not solely affected by PV annular size. The findings of this study will have more clinical relevance in the setting of transpulmonary stent implantation or future advent of transcatheter valve replacement where precise sizing and deployment of the implant are pivotal to positive clinical outcome and avoidance of complications.

The study has several limitations. The small sample size can underpower statistical analyses and the resultant statistics may not be a close representation to the true population. Due to the retrospective design, biases in case selection cannot be excluded where only dogs with preservation of all anatomic components of the PV were selected. The OFPs defined in this study may not apply to severely dysplastic PVs that have partially or completely lost their organic architecture as a semilunar valve. Third, the CCT and anesthetic protocols for the two groups were not standardized *a priori* and did have differences, which may affect the quality and variability of the data. Nonetheless, the CCT and associated anesthetic protocols in the PS group are dedicated

to dogs with PS and have been routinely performed at the authors' institution for several years. Last, there was an apparent difference in breed composition between the healthy and PS groups. This is mostly due to the high prevalence of PS in brachycephalic breeds and that no healthy brachycephalic dogs were enrolled in the other study from which the normal dogs were obtained. In light of the common perception that brachycephalic dogs have a barrel chest conformation, we did not identify a difference in chest conformation (TDTWR) between these two groups, which has been considered a major source of variability in previous studies measuring cardiac dimensions on thoracic radiographs [17,18]. Regardless, the differences found may reflect differences in breed (brachycephalic) and not disease state (PS).

2.5 Conclusion

Optimized projections of the pulmonary valve were different between apparently healthy dogs and dogs with severe PS. The CO projection appears to be the optimal fluoroscopic view of the PV to obtain during TPVI in dogs with severe PS. Measurements of PV diameter by TTE may not accurately represent the effective diameter of the PV as determined by CCT. The findings of this study may be useful for device sizing and intra-procedure guidance of TPVI as veterinary interventional cardiology continues to evolve.

TABLES AND FIGURES – CHAPTER 2

Table 2.1: Summary of the study groups. The dogs in the pulmonary stenosis (PS) group were smaller in body weight but not different in age and thoracic conformation compared to the normal group. The majority of the PS group were French bulldogs whereas no brachycephalic breeds were included in the normal group. FI, female intact; FS, female spayed; MC, male castrated; MI, male intact; TDTWR, thoracic depth-to-width ratio.

	Normal (n=18)	PS (n=18)	*p* value
Age (years)	3.5 (1 - 10)	1 (0.42 - 7)	0.8248
Sex	7 MC; 11 FS	6 FI, 3 FS; 8 MI, 1 MC	
Body weight (kg)	23.16 (8.12 - 33)	11.26 (6- 18)	<0.0001
TDTWR	0.87 (0.6 - 1)	0.67 (0.56 – 0.99)	0.1948
Breed	Ten mixed breed, two Staffordshire Bull Terrier, two Labrador Retriever, one Golden Retriever, one Cardigan Welsh Corgi, one Doberman Pinscher, one Italian Greyhound	Fifteen French bulldogs, one Australian Shepherd, one English bulldog, one Miniature Schnauzer	

Table 2.2: Optimized fluoroscopic projections (mean and 95% confidence in degrees) of the pulmonary valve annulus in 18 healthy dogs and 18 dogs with congenital pulmonary valve stenosis (PS). CAU, caudal; CRA, cranial; LAO, left anterior oblique; RAO, right anterior oblique.

		Normal (n = 18)		PS (n = 18)		p values
En face	Mean	RAO 7	CAU 14	RAO 26	CAU 19	0.104
	95%	RAO 0-15	CAU 7-21	RAO 18-34	CAU 12-27	
Cusp-overlap	Mean	LAO 85	CAU 4	LAO 62	CRA 5	0.017
	95%	LAO 78-91	CRA 2-CAU 11	LAO 54-70	CRA 13-CAU 4	
Coplanar	Mean	RAO 87	CRA 38	LAO 71	CAU 21	<0.001
	95%	RAO 79-96	CRA 31-44	LAO 63-79	CAU 14-28	

Table 2.3: Summary of Bland-Altman statistics. The pulmonary valve diameters were measured in millimeters. CI, confidence interval; LOE, limits of agreement; PV_{eff}, effective pulmonary valve diameter; PV_{CO}, pulmonary valve diameter measured on cusp-overlap projection; PV_{Angio}, pulmonary valve diameter measured on angiocardiogram; PV_{CP}, pulmonary valve diameter measured on coplanar projection; PV_{TTE}, pulmonary valve diameter measured on transthoracic echocardiogram.

Comparison (mm)	Mean difference	95% CI	Upper LOE	Lower LOE
PV_{eff} - PV_{CO}	-0.08	-0.36 – 0.19	1.01	-1.17
PV_{eff} - PV_{CP}	-0.17	-0.50 – 0.16	1.13	-1.48
PV_{eff} - PV_{TTE}	1.89	1.27 – 2.52	4.35	-0.56
PV_{eff} - PV_{Angio}	0.11	-0.30 – 0.53	1.74	-1.52

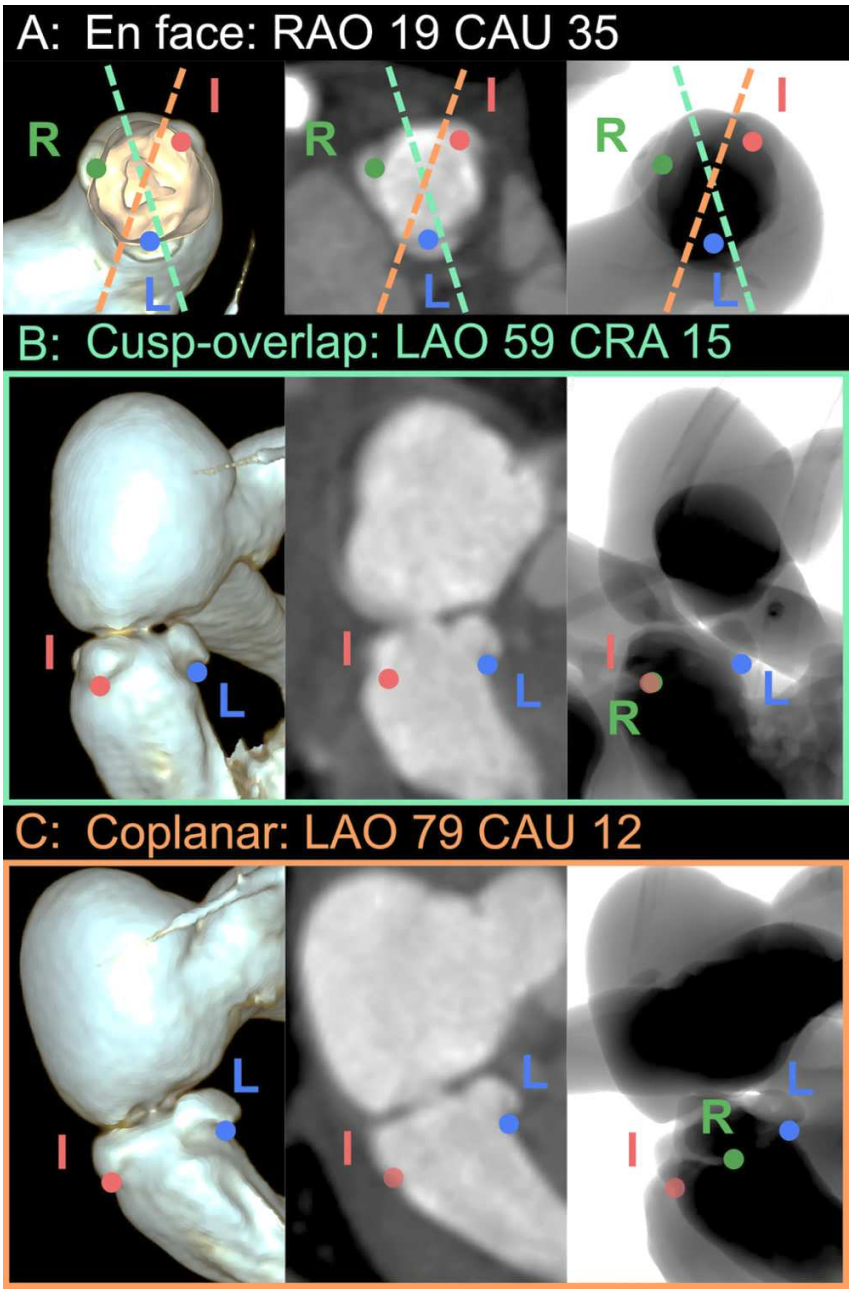

Figure 2.1: Optimized fluoroscopic projections of the pulmonary valve. Panel A: Volume-rendered, multiplanar reformat, and virtual fluoroscopic image of the *en face* projection. The nadirs of the intermediate (red marker, I), left (blue marker, L), and right (green marker, R) cusps are marked. The imaging planes for the cusp overlap view (orange dashed line) and the coplanar view (cyan dashed line) are also marked. Panel B: Volume-rendered, multiplanar reformat, and virtual fluoroscopic image of the cusp-overlap view. This projection isolates the left sinus caudally (blue marker) with overlapping of the right (green marker) and intermediate (red marker) sinuses. Panel C: Volume-rendered, multiplanar reformat, and virtual fluoroscopic image of the coplanar view. There is central positioning of the right sinus (green marker) with all three cusps forming a straight line to represent the virtual annulus. CAU, caudal; CRA, cranial; LAO, left anterior oblique; RAO, right anterior oblique.

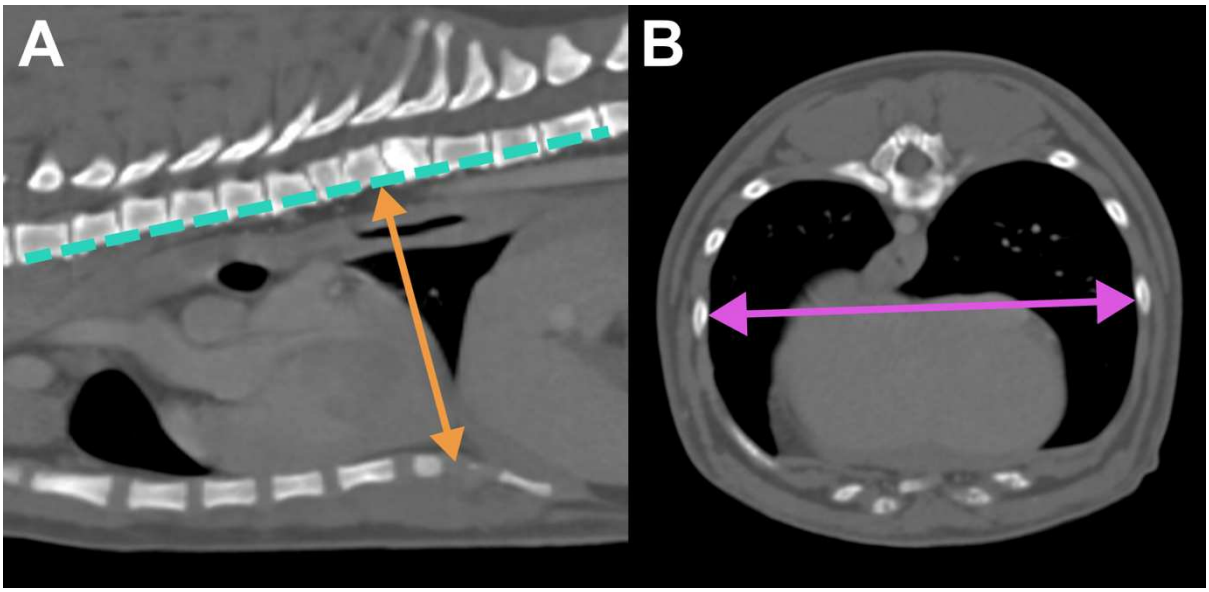

Figure 2.2: Thoracic depth (orange double-head arrow) is measured on the central sagittal plane in multiplanar reformatting (A) from the cranial edge of the xiphoid process to the ventral border of the vertebral column (cyan dashed line). Thoracic width (purple double-head arrow) is measured on the transverse plan at the level of the eighth rib (B) as the linear dimension between the medial borders of the eighth ribs at their peak curvatures.

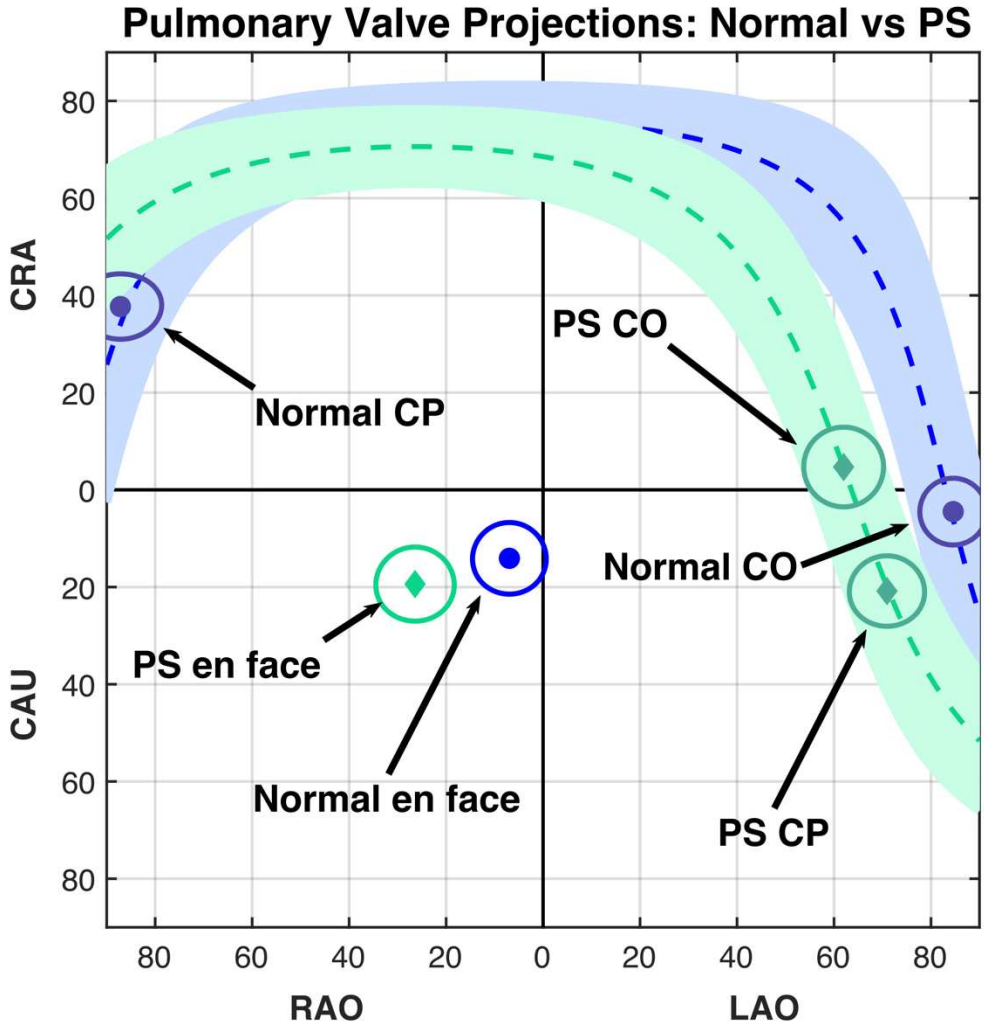

Figure 2.3: Fluoroscopic geography of the optimized fluoroscopic projections of the pulmonary valve in healthy dogs (dot markers) and dogs with severe pulmonary stenosis (diamond markers). The plot only shows projections with the detector of the C-arm above the fluoroscopic table (LAO 90 – RAO 90; CRA 90 – CAU 90). The means and cones of 95% confidence of the *en face,* cusp-overlap, and coplanar views are shown together with the means and 95% confidence area of the S curves. CAU, caudal; CO, cusp-overlap; CP, coplanar; CRA, cranial; LAO, left anterior oblique; PS, pulmonary stenosis; RAO, right anterior oblique.

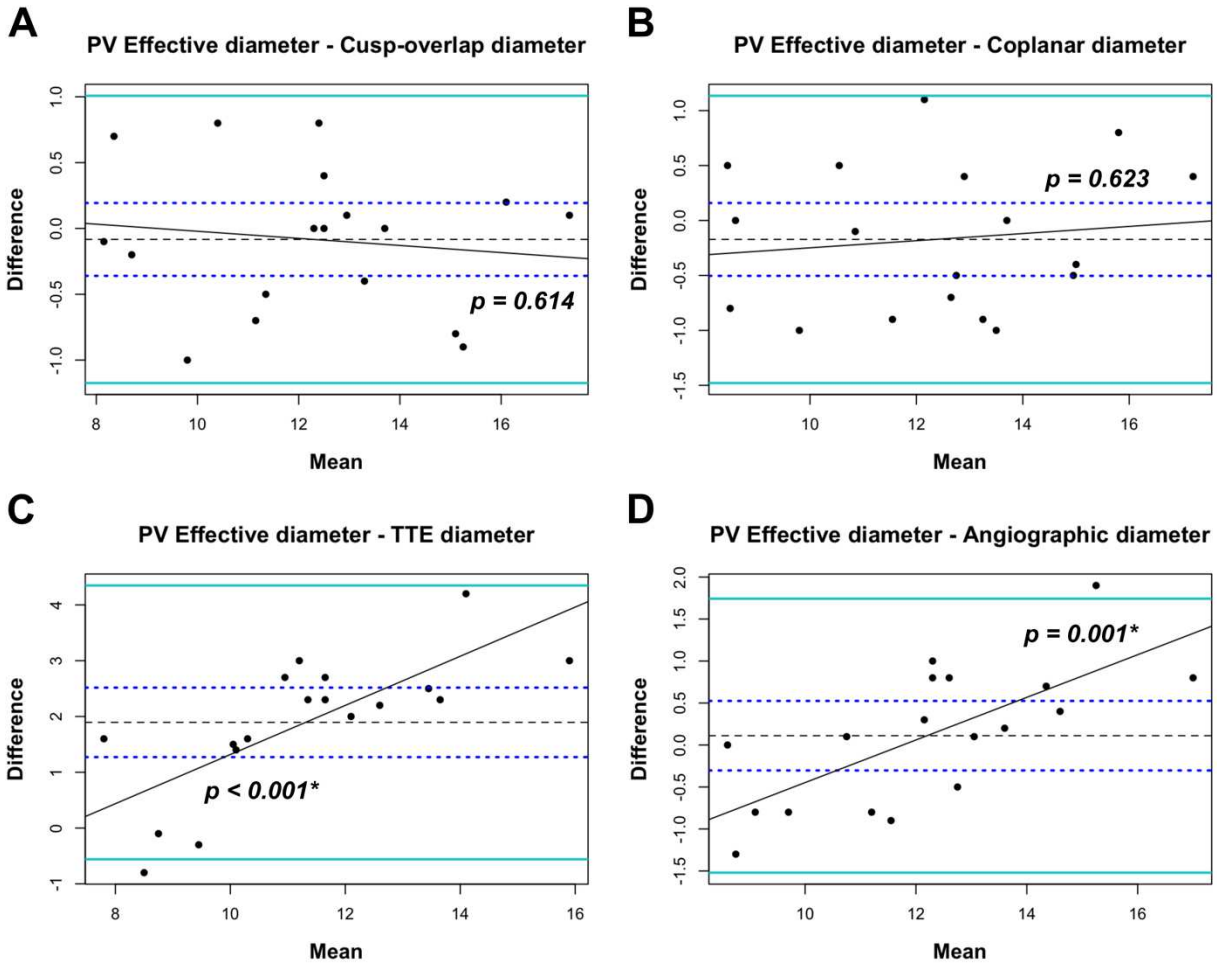

Figure 2.4: Bland-Altman analyses between different measurements of the pulmonary annular diameter. (A) Agreement between the mean effective diameter and the mean diameter measured on the cusp-overlap view. No systemic bias was detected with narrow limits of agreement. (B) Agreement between the mean effective diameter and the mean diameter measured on the coplanar view. No systemic bias was detected with narrow limits of agreement. (C) Agreement between the mean effective diameter and the mean diameter measured on transthoracic echocardiography. There is positive systemic bias with wide limits of agreement and proportional bias as data values increased ($p < 0.001$). (D) Agreement between the mean effective diameter and the mean diameter measured on intra-operative angiocardiography. No systemic bias was noted but proportional bias was present ($p = 0.001$).

REFERENCES – CHAPTER 2

[1] Pighi M, Thériault-Lauzier P, Alosaimi H, Spaziano M, Martucci G, Xiong T-Y, Buithieu J, Ybarra LF, Afilalo J, Leipsic J, Ozden Tok O, Mousavi N, Mangiameli A, Pilgrim T, Praz F, Windecker S, Piazza N. Fluoroscopic anatomy of right-sided heart structures for transcatheter interventions. JACC: Cardiovascular Interventions 2018;11:1614–25.

[2] Thériault-Lauzier P, Andalib A, Martucci G, Mylotte D, Cecere R, Lange R, Tchétché D, Modine T, Van Mieghem N, Windecker S, Buithieu J, Piazza N. Fluoroscopic anatomy of left-sided heart structures for transcatheter interventions. JACC: Cardiovascular Interventions 2014;7:947–57.

[3] Spaziano M, Thériault-Lauzier P, Meti N, Vaquerizo B, Blanke P, Deli-Hussein J, Chetrit M, Galatas C, Buithieu J, Lange R, Martucci G, Leipsic J, Piazza N. Optimal fluoroscopic viewing angles of left-sided heart structures in patients with aortic stenosis and mitral regurgitation based on multislice computed tomography. Journal of Cardiovascular Computed Tomography 2016;10:162–72.

[4] Zgheib A, Campens L, Abualsaud A, Al Isma'ili A, Barbanti M, Dvir D, Gada H, Granada JF, Latib A, Leipsic J, Maisano F, Martucci G, Medina De Chazal HA, Modine T, Mylotte D, Prendergast B, Sawaya F, Spaziano M, Tang G, Theriault-Lauzier P, Tchetche D, Van Mieghem N, Søndergaard L, De Backer O, Piazza N. Aortic annulus s-curve. JACC: Cardiovascular Interventions 2022;15:2353–73.

[5] Sá JPM de. Applied statistics: using SPSS, Statistica, MATLAB, and R. 2nd ed. Berlin ; New York: Springer; 2007.

[6] Blanke P, Weir-McCall JR, Achenbach S, Delgado V, Hausleiter J, Jilaihawi H, Marwan M, Norgaard BL, Piazza N. Computed tomography imaging in the context of transcatheter aortic valve implantation (TAVI) / transcatheter aortic valve replacement (TAVR): An expert consensus document of the Society of Cardiovascular Computed Tomography. Journal of Cardiovascular Computed Tomography 2019;13:1–20.

[7] Scansen BA. Advances in the treatment of pulmonary valve stenosis. Vet Clin North Am Small Anim Pract 2023;53:1393–414.

[8] Santarelli G, Bouvard J, Brethel SF, Gordon S, Lord S, Mavropoulou A, Oliveira P, Sykes KT, Swift S, Culshaw GJ. Non-cardiogenic pulmonary oedema complicating balloon valvuloplasty and stent angioplasty of severe pulmonary valve stenosis in four dogs. J Vet Cardiol 2022;39:79–88.

[9] Sosa I, Swift ST, Jones AE, Estrada AH, Fudge JC. Stent angioplasty for treatment of canine valvular pulmonic stenosis. J Vet Cardiol 2019;21:41–8.

[10] Ciccozzi M, Stauthammer CD, Gavic E, Masters A. Trans-pulmonary stent placement for pulmonary stenosis in a dog with a type R2A coronary artery anomaly. J Vet Cardiol 2024;55:19–25.

[11] Markovic LE, Whipp C, Morgan K, Almeida D, Hiremath G. Transpulmonary stent implantation for dysplastic pulmonary valve stenosis with a single left coronary ostium and anomalous prepulmonary right coronary artery in an english bulldog. CASE (Phila) 2020;4:540–5.

[12] Borgeat K, Gomart S, Kilkenny E, Chanoit G, Hezzell MJ, Payne JR. Transvalvular pulmonic stent angioplasty: procedural outcomes and complications in 15 dogs with pulmonic stenosis. J Vet Cardiol 2021;38:1–11.

[13] Borenstein N, Chetboul V, Passavin P, Morlet A, Fernandez-Parra R, Carazo Arias LE, Giannettoni G, Saponaro V, Poissonnier C, Ghazal S, Lefort S, Trehiou-Sechi E, Marchal CR, Delle Cave J, Vannucci E, Behr L, Verwaerde P. Successful transcatheter pulmonary valve implantation in a dog: first clinical report. J Vet Cardiol 2019;26:10–8.

[14] Terrade G, Borenstein N, Chetboul V, Toma C, Guillaume E, Bruneval P, Fiette L, Carazo Arias LE, Morlet A, Le Dudal M. First reported long-term two- and three-dimensional echocardiographic follow-up with histopathological analysis of a transcatheter pulmonary valve implantation in a pet dog. J Vet Cardiol 2024;53:52–9.

[15] Soszyn N, Shorofsky M, Franco SR, Zablah JE, Morgan GJ. Computed tomography-derived normative values and z-scores of the pulmonary valve annulus and sino-tubular junction in the pediatric population. Journal of Cardiovascular Computed Tomography 2024;18:489–93.

[16] Curran L, Agrawal H, Kallianos K, Kheiwa A, Lin S, Ordovas K, Mahadevan VS. Computed tomography guided sizing for transcatheter pulmonary valve replacement. Int J Cardiol Heart Vasc 2020;29:100523.

[17] Buchanan JW, Bücheler J. Vertebral scale system to measure canine heart size in radiographs. J Am Vet Med Assoc 1995;206:194–9.

[18] Bodh D, Hoque M, Saxena AC, Gugjoo MB, Bist D, Chaudhary JK. Vertebral scale system to measure heart size in thoracic radiographs of Indian Spitz, Labrador retriever and Mongrel dogs. Vet World 2016;9:371–6.

CHAPTER 3: EFFECTS OF PIMOBENDAN ON MITRAL ANNULAR DYNAMICS AND SEVERITY OF MITRAL REGURGITATION IN DOGS WITH SUBCLINICAL DEGENERATIVE MITRAL VALVE DISEASE AS DETERMINED BY CARDIAC COMPUTED TOMOGRAPHY

3.1 Introduction

Pimobendan, an inodilator acting through phosphodiesterase-III inhibition and calcium sensitization, is part of the guideline-directed medical management of degenerative mitral valve disease (DMVD) in dogs. Pimobendan has been shown to prolong survival and time to onset of congestive heart failure in dogs with subclinical DMVD and left heart enlargement (American College of Veterinary Internal Medicine [ACVIM] Stage B2) [1]. Reduction in left heart size and severity of mitral regurgitation (MR) after administration of pimobendan has also been reported in dogs with subclinical DMVD [2,3]. It has been speculated that administration of pimobendan promotes left ventricular (LV) forward stroke volume (FSV) through afterload reduction (systemic vasodilation) and positive inotropy [3,4]. Validation of this hypothesis has not been performed in dogs with naturally occurring DMVD; other hemodynamic or biomechanical mechanisms of pimobendan's clinical benefit may exist.

The geometry and size of the mitral annulus (MA) is critical to the biomechanical function of the MV and can become abnormal in dogs with DMVD [5,6]. Moreover, the MA is not a static structure but a dynamic, functional component of the mitral apparatus. The capacity of the MA to change its shape and size throughout the cardiac cycle is defined as mitral annular dynamics (MAD). Abnormal MAD have been documented in people with degenerative mitral regurgitation (MR) where the MA undergoes systolic expansion instead of constriction [7–10]. This has been

associated with a dynamic increase in regurgitant orifice area throughout ventricular systole[7–11]. Given the known association between MR and MAD, the potential influence of pimobendan on MAD is of relevance in understanding the pathophysiology of this drug in dogs with DMVD.

The advent of cardiac-gating and multidetector computed tomography (CT) has made it feasible to capture cardiac motion, quantify cardiac chambers, and characterize the conformational changes of cardiac structures at different cardiac phases with excellent spatial and temporal resolution. These features make cardiac computed tomography (CCT) a potentially useful imaging modality for cardiac volume quantification and characterization of MAD in dogs, aided by state-of-the-art imaging software. The goal of this study was to investigate the short-term effect of pimobendan on MAD, severity of MR, and indirect estimates of systemic arterial compliance in a small group of dogs with newly diagnosed ACVIM stage B2 DMVD using CCT. We hypothesized that pimobendan reduces the severity of MR by enhancing left ventricular contractile function and systolic contraction of the MA, and that pimobendan will not change indirect estimates of systemic arterial compliance.

3.2 Material and method

3.2.1 Animals and study design

Client-owned dogs with newly diagnosed ACVIM stage B2 DMVD were prospectively enrolled. All dogs were larger than 4 kg in body weight to ensure optimal spatial resolution of the CCT. The dogs were otherwise healthy and not receiving pimobendan or other medications with known cardiovascular effect at the time of enrollment. At the first study visit, physical examination, complete blood count, diagnostic chemistry profile, and thoracic radiographs were performed to confirm absence of major comorbidities. A comprehensive transthoracic echocardiographic exam

and CCT were acquired under brief sedation. The patient was then discharged with oral pimobendan at 0.5-0.6 mg/kg/day divided into twice daily dosing. All dogs returned 14 days after the first visit for repeat echocardiogram and CCT under the same sedation and imaging protocols. At the end of the second visit, all dogs were discharged to the owner and maintained on chronic pimobendan therapy at the same dosage. The study protocol was approved by the Institutional Animal Care and Use Committee at Colorado State University (protocol number 1612).

3.2.2 Echocardiography

Standard two-dimensional and Doppler echocardiography was performed at both study visits (before and after initiation of pimobendan therapy). All dogs received butorphanol 0.1-0.3 mg/kg IV for the echocardiographic exam. The diagnosis of ACVIM stage B2 DMVD was made according to the ACVIM consensus guidelines for the diagnosis and treatment of DMVD in dogs [12]. Absence of significant semilunar valve disease or other structural abnormalities was confirmed in all dogs. Special attention was paid to ensure the absence of hemodynamically relevant tricuspid regurgitation and right heart enlargement despite the presence of tricuspid valve degeneration. An estimate of arterial elastance (Ea) was acquired as previously described in another veterinary study [13]. Echocardiographic Ea was calculated as mean oscillometric blood pressure divided by the LV forward stroke volume (aortic velocity-time integral × aortic valve cross-sectional area) indexed to body weight in kilograms.

3.2.3 Cardiac computed tomography – Image acquisition

A dual source, 384-slice (192 slices in each detector row) computed tomography scanner (SOMATOM Force, Siemens Healthineers USA) was used to acquire all CCT studies. All CCTs were acquired under brief sedation and spontaneous respiration. The sedatives were administered (butorphanol 0.2 to 0.5 mg/kg IV with titrated boluses of alfaxalone 0.5 to 1 mg/kg IV) and

sedation monitored by the Anesthesia and Pain Management Service at the authors' institution. The dogs were positioned on the CT table in ventral recumbency with flow-by oxygen supplementation. Pulse rate, peripheral oxygen saturation, and oscillometric blood pressure were monitored during the CCT.

A pre-contrast thoracic CT was first acquired and reconstructed in order to select the monitoring slice for bolus tracking. The region of interest with a threshold of 150 Hounsfield units was placed in the aortic arch to trigger retrospective acquisition of the levophase, and then the dextrophase after an 8 to 12 second delay based on the patient's heart rate. A triphasic contrast (iohexol 300 mgI/mL, Omnipaque, GE Healthcare) protocol delivering a total of 1.5 ml/kg contrast was used: 1 mL/kg of 100% contrast at 1 to 3 ml/s (0.21 +/- 0.07 ml/kg/s), followed by 1 mL/kg of 50% contrast/saline mixture at 1 to 3 ml/s (0.21 +/- 0.07 ml/kg/s), and a final 1 mL/kg saline bolus at 1 to 3 ml/s. All studies were reconstructed at 0.75 mm slice thickness with the field-of-view containing the entire heart and great vessels. Both the levophase and dextrophase scans were reconstructed into 20 phases at 5% increments of the R-to-R cycle length and stored for further analysis.

3.2.4 Cardiac computed tomography – Image analysis

The MA was manually segmented using a dedicated CCT imaging software (3mensio Structural Heart, Pie Medical Imaging, the Netherlands). A total of 16 markers were placed around the MA in multiplanar reformatting to generate a three-dimensional (3D), saddle-shaped MA ring (**Figure 1**). The left/lateral and right/medial fibrous trigones were manually identified. After successful segmentation of the MA, the following geometrical measurements were auto-generated: mitral annular area (MAA), aortoparietal distance (APD), intercommissural distance (ICD), and trigone-to-trigone distance (TTD). In addition to the automated measurements, the sphericity index (SI) of

the MA was calculated as APD/ICD. Leaflet-to-annular index (LAI) was calculated as a measure of MV leaflet coaptation reserve described in previous human and veterinary literature [14–16]. The lengths of the aortic and parietal MV leaflets were measured across the center of the MV and summated as the total leaflet length (TLL). The LAI was defined as TLL/APD.

Volumetric measurements of CCT were made with an offline imaging software (IntelliSpace Portal, Philips Healthcare USA). LV end-diastolic (LVEDV) and end-systolic (LVESV) volumes were measured to quantify LV total stroke volume (TSV) and ejection fraction (EF). Right ventricular total stroke volume was used as a surrogate for LV forward stroke volume (FSV) in the absence of relevant right-sided valvular regurgitation. As a result, the regurgitant volume (RVol) across the MV was estimated by difference between the left and right ventricular TSVs. Regurgitant fraction (RF) was calculated as RVol/LVTSV. Left atrial end-diastolic (LAEDV) and end-systolic (LAESV) volumes were measured with exclusion of the left atrial appendage and pulmonary veins. All linear, area, and volumetric measurements were indexed to (body weight in kilograms)$^{1/3}$, body surface area (in meters squared), and body weight (in kilograms) respectively. Measurements of MA geometry and volumes were made at different cardiac phases: Mid-diastole (the beginning of diastasis), late-diastole (right before atrial contraction), end-diastole (after atrial contraction and before onset of ventricular systole), mid-systole (first phase of aortic valve opening), and end-systole (at minimal LV volume). In addition, a late systolic phase between the mid- and end-systole was selected to measure the LAI (**Figure 2**).

Systemic arterial compliance was estimated by the aortic distensibility index (ADI) [17,18]. The ADI is defined as the fractional cross-sectional area change in the ascending aorta (at the middle point between the sinotubular junction of the aortic valve and the origin of the

brachycephalic trunk) divided by systemic pulse pressure (oscillometric systolic arterial pressure – diastolic arterial pressure).

3.2.5 Statistics

All continuous variables were examined for normality using Shapiro-Wilk test and normal quantile-quantile plot. Continuous variables are summarized as mean ± standard deviation or median with interquartile range for parametric and non-parametric sample data. Paired statistical methods were used for repeated measurements on the same dogs at different timepoints (before and after the administration of pimobendan). Paired t-test or Wilcoxon signed rank test were used to compare means or medians between the two timepoints depending on normality of the difference in measurements. The significance level (alpha) of the study is set at 0.05. Statistical computing and graphics were compiled using an open-source programming language and software environment (R version 4.4.1 [Race for your life]; RStudio version 2024.09.0+375).

3.3 Results

3.3.1 Study sample

Twenty client-owned dogs of various breeds were enrolled at Colorado State University Veterinary Teaching Hospital (**Table 1**) between February 2022 and September 2023. All dogs had unremarkable blood work and no major extracardiac abnormalities on thoracic radiographs at baseline. The mean dosage of oral pimobendan was 0.57 mg/kg/day ranging between 0.5 to 0.64 mg/kg/day. All dogs received twice daily oral pimobendan for the entire study period and completed the study without discontinuation of medication or major adverse events (only one dog experienced mild, self-limiting diarrhea). No dogs developed signs of congestive heart failure or overt disease progression during the study period.

3.3.2 The effect of pimobendan on mitral annular dynamics

At baseline, the MA reached its minimal size at end-diastole (after atrial contraction) and then underwent systolic expansion (**Figure 3**). This pattern was observed in MAA and ICD but was most prominent in APD where the end-systolic dimension exceeded the diastolic dimension (**Figure 3B**). The TTD remained unchanged throughout the cardiac cycle (**Figure 3D**). Short term administration of pimobendan decreased the mean end-systolic MAA ($p < 0.0001$) and APD ($p < 0.0005$) whereas the mean ICD was reduced at both mid-systole ($p = 0.044$) and end-systole ($p < 0.0001$). The were no change in mean end-diastolic MAA ($p = 0.064$), APD ($p = 0.2025$), and ICD ($p = 0.0675$). No differences were noted on mean TTD or SI at any cardiac phase. Last, the mean LAI increased ($p = 0.0017$) due to reduction in APD at late systole ($p = 0.0039$) with unchanged TLL ($p = 0.595$) (**Figure 4F**). Paired statistics of MAD changes are summarized in **Table 2**.

3.3.3 The effect of pimobendan on mitral regurgitation and left heart volumes

There was a reduction in mean LVEDV ($p = 0.0016$) by 12.4% and LVESV ($p = 0.0015$) by 18.4% (Figure 4A and 4B) after pimobendan. Mean left ventricular TSV reduced ($p = 0.044$) while the mean LVEF remained unchanged ($p = 0.15$). Both the mean RVol ($p = 0.0027$) and RF ($p < 0.001$) decreased by approximately 30% (**Figure 4C and 4D**). Left atrial volume at both end-diastole ($p = 0.0014$) and end-systole ($p < 0.001$) reduced by 9.4% and 22.2% (**Figure 4E**) respectively. Paired statistics of changes in volumetric measurements are summarized in **Table 3**.

3.3.4 The effect of pimobendan on estimates of LV afterload

Both the echocardiographic Ea ($p = 0.365$) and ADI ($p = 0.648$) measured on CCT did not change after pimobendan therapy. There was also no difference in mean blood pressure ($p = 0.504$) between the two visits (**Table 3**).

3.4 Discussion

This study found that short-term pimobendan therapy reduced the severity of MR by augmenting systolic contraction of the MA, resulting in a pharmacologic annuloplasty and limiting the size of the regurgitant orifice. Similar observations have been reported in humans where dobutamine infusion reduced the mitral annular diameter and severity of MR without concurrent systemic vasodilation [19]. Previous animal studies have also found an association between LV systolic function and the regurgitant orifice area of experimentally induced MR [20,21].

The MV is a highly dynamic structure with complex anatomy and biomechanics. Rather than an organic anatomic structure, the canine MA can be considered a "virtual" structure consisting of the aortomitral fibrous continuity (the aortic portion) and the myocardial conjunction of the LA and LV (the parietal portion) [22]. Due to the fibrous and fixed nature of the trigones, the TTD of the MA does not undergo much change throughout the cardiac cycle (**Figure 3**). Rather, the parietal portion of the MA changes its size and shape with dilation and contraction of the LA and LV myocardium. The dynamics of the MA plays an important role in the biomechanical function of MV. An experimental canine study showed that the shape and size of the MA in healthy dogs are influenced by both atrial and ventricular contractions throughout the cardiac cycle [23]. During atrial contraction, contraction of the MA occurs substantially to facilitate leaflet coaptation and closure right before the onset of ventricular systole. The MA will continue to contract in ventricular systole to further optimize MV coaptation and reduce the amount of mechanical stress on the leaflets and subvalvular apparatus. The normal MAD can be affected by changes in LA or LV contractile function, loading condition of the left heart, and presence of MR [23].

All dogs in our study showed abnormal MAD with the MA undergoing systolic expansion instead of contraction, especially in the aortoparietal dimension (**Figure 3**). This specific pattern of abnormal MAD is also shared by people with DMVD as described in multiple studies [7–11]. The timing of the paradoxical increase in MA dimension is coincident with the rapid expansion of LA volume secondary to MR, which can further worsen malcoaptation of the MV leaflets and MR during ventricular systole [24]. This may, at least partially, explain the late systolic peaking in regurgitant orifice area of MR as observed in people [25–28] and likely in dogs (**Figure 2**). As shown in our study, pimobendan rectified systolic expansion of the MA, which theoretically mitigates the functional/dynamic expansion of the regurgitant orifice area (so-called pharmacologic annuloplasty) [19]. The increase in late-systolic LAI can also be considered indirect evidence of this phenomenon where a smaller annular area is now covered by the same amount of leaflet length as existed at baseline. This effect is independent of the absolute size of the MA as there is no significant change in the mean diastolic dimensions of the MA after receiving pimobendan despite the reduction in mean LVEDV and LAEDV.

Segmenting and tracking a dynamic 3D structure like the MA can be challenging for cardiac imaging modalities. Previous veterinary studies have utilized real-time 3D transthoracic and transesophageal echocardiography to determine MA morphology in dogs but are limited to a single-phase analysis in systole [5,6,29]. While echocardiography provides high resolution imaging of the valve leaflets, cross-sectional imaging such as CCT provides a wider field of view including the entire left heart and all functional components of the mitral apparatus. The use of CCT has been reported in many veterinary studies but none have utilized the technology to study the MV apparatus in dogs with DMVD. This study demonstrates that detailed geometrical assessment of the canine MA at multiple cardiac phases is feasible with the use of CCT. Future

studies are in need to explore other applications of CCT in canine DMVD such as perioperative imaging for planning and evaluating surgical/transcatheter interventions.

The capability to quantify cardiac chamber volumes also affords CCT a role in the quantification of MR. The volumetric quantification method used to obtain RVol and RF in this study was adopted from previous studies in people with DMVD [30]. With isolated MR, the difference in TSV between the left and right ventricles should equal to the RVol assuming the FSV is the same out of the pulmonary and aortic outflow tracts. With the technical challenges in performing cardiac magnetic resonance imaging for MR quantification in dogs [31], quantification of RVol using CCT should be considered as a viable alternative.

There were no significant changes in mean blood pressure, echocardiographic Ea, and ADI (**Table 3**); therefore, systemic vasodilation appears less likely a meaningful mechanism for MR reduction after pimobendan therapy. Notably, it is equally possible that these estimates of vascular tone are insensitive.

There are a few limitations relevant to this study. First, the study only represents the short-term effect of pimobendan administration. Future studies of longer duration would be required to understand if the pharmacological effect persists to later stages of the disease. Second, the small sample size can underpower the statistical analyses performed in this study. Third, the indirect estimations of systemic arterial compliance in the study were not validated by any form of reference method in dogs. Oscillometric blood pressure measurement in the dog is also known to have inaccurate or imprecise readings [32]. Lastly, the study only focuses on the dynamics of the MA and does not address other components of the mitral apparatus such as valve leaflets, chordae tendineae, or papillary muscles. It is still possible that pimobendan also affects MR severity through biomechanical influence on these structures.

3.5 Conclusion

In conclusion, we find that pimobendan in subclinical dogs with DMVD augments systolic contraction of the mitral annulus, reversing the detrimental effect of end-systolic expansion that occurs with MR. We postulate that this mechanical benefit, or pharmacologic annuloplasty, helps to explain the clinical benefit and reduction in heart size seen in prior studies [1,3]. Greater understanding of the mechanistic benefit of pimobendan may facilitate refinement of the clinical indication for this therapy in dogs.

TABLES AND FIGURES – CHAPTER 3

Table 3.1: Demographics of the study sample presented as mean (range of data). LA/Ao, left atrium-to-aortic dimension ratio; LVIDdN, normalized left ventricular internal dimension in diastole.

	All dogs (n = 20)
Age (years)	10.38 (6-14)
Sex	Male 13, Female 7
Body weight (kg)	9.84 (4.3-19.6)
LVIDdN	1.84 (1.7-2.05)
LA/Ao	1.83 (1.61-2.5)
Pimobendan (mg/kg/day)	0.57 (0.5-0.64)
Breed	Border Collie (1), Boston Terrier (1), Cavalier King Charles Spaniels (4), Chihuahua (1), Havanese (2), Mixed breed (10), Yorkshire Terrier (1)

Table 3.2: Geometrical measurements of the mitral annulus before and after pimobendan at difference cardiac phases with p values representing change pre to post pimobendan therapy. APD, aortoparietal distance; ED, end diastole; ES, end systole; ICD, intercommissural distance; LD, late diastole; MAA, mitral annular area; MD, mid diastole; MS, mid systole; SD, standard deviation; SI, sphericity index; TTD, trigone-to-trigone distance. All linear and area measurements were indexed to (body weight in kilograms)$^{1/3}$ and body surface area (in meters squared) respectively. *p values reaching statistical significance ($p < 0.05$)

Measurement	Timepoint	Cardiac Phase									
		MD		LD		ED		MS		ES	
		Mean±SD	p value	Mean±SD	p value	Mean±SD	p value	Mean±SD	p value	Mean±SD	p value
MAA	Pre	10.28±1.39	0.3912	10.45±1.47	0.3713	8.72±1.43	0.0645	9.69±1.81	0.1564	9.56±2.08	<0.001*
	Post	10.09±1.61		10.23±1.78		8.39±1.26		9.32±1.97		8.19±1.67	
APD	Pre	10.68±0.93	0.6439	10.85±0.99	0.4043	9.75±0.93	0.2025	10.52±1.39	0.8615	10.96±1.49	<0.001*
	Post	10.59±1.23		10.69±1.30		9.54±0.99		10.56±1.43		9.93±1.30	
ICD	Pre	12.10±0.94	0.2186	12.17±0.87	0.3236	11.18±0.97	0.0675	11.57±0.96	0.0438*	11.32±1.19	<0.001*
	Post	11.87±0.94		12.00±1.10		10.86±0.99		11.29±1.08		10.57±0.99	
TTD	Pre	6.21±0.58	0.0906	6.36±0.53	0.9283	6.17±0.56	0.8597	6.28±0.61	0.0697	6.28±0.78	0.0518
	Post	6.40±0.61		6.35±0.65		6.19±0.64		6.09±0.67		6.02±0.64	
SI	Pre	0.88±0.07	0.6028	0.89±0.07	0.9152	0.87±0.06	0.6575	0.91±0.07	0.0842	0.97±0.08	0.0795
	Post	0.89±0.09		0.89±0.09		0.88±0.08		0.94±0.09		0.94±0.09	

Tablet 3.3: Comparisons of left heart size, severity of mitral regurgitation, and systemic blood pressure and arterial compliance before and after pimobendan. Abbreviations: ADI, aortic distensibility index; Ea, arterial elastance; LAEDV, left atrial end diastolic volume; LAESV, left atrial end systolic volume; LAI, leaflet-to-annulus index; LVEDV, left ventricular end diastolic volume; LVEF, left ventricular ejection fraction; LVESV, left ventricular end systolic volume; LVSV, left ventricular stroke volume; MBP, mean blood pressure; RF, regurgitant fraction; RVol, regurgitant volume; SD, standard deviation. *p values reaching statistical significance ($p < 0.05$).

Measurement	Timepoint	Mean±SD	p value
LAI	Pre	1.21±0.10	0.0017*
	Post	1.26±0.08	
LVEDV (mL/kg)	Pre	4.21±0.80	0.0017*
	Post	3.69±0.86	
LVESV (mL/kg)	Pre	1.52±0.35	0.0015*
	Post	1.24±0.38	
LVEF (%)	Pre	64.01±5.24	0.1498
	Post	66.44±6.92	
LVSV (mL/kg)	Pre	2.7±0.58	0.0445*
	Post	2.45±0.61	
RVol (mL/kg)	Pre	1.04±0.52	0.0027*
	Post	0.73±0.50	
RF (%)	Pre	37.1±11.04	0.0003*
	Post	27.35±12.22	
LAESV (mL/kg)	Pre	1.94±0.69	0.0006*
	Post	1.51, 1.125-1.833	
LAEDV (mL/kg)	Pre	0.96±0.30	0.0014*
	Post	0.78±0.24	
Ea (mmHg/mL/kg)	Pre	64.55±18.94	0.365
	Post	60.81±20.01	
ADI ($mmHg^{-1}x10^3$)	Pre	5.379, 4.456-6.616	0.6477
	Post	5.15±1.48	
MBP (mmHg)	Pre	89.50±22.76	0.5038
	Post	93.25±11.82	

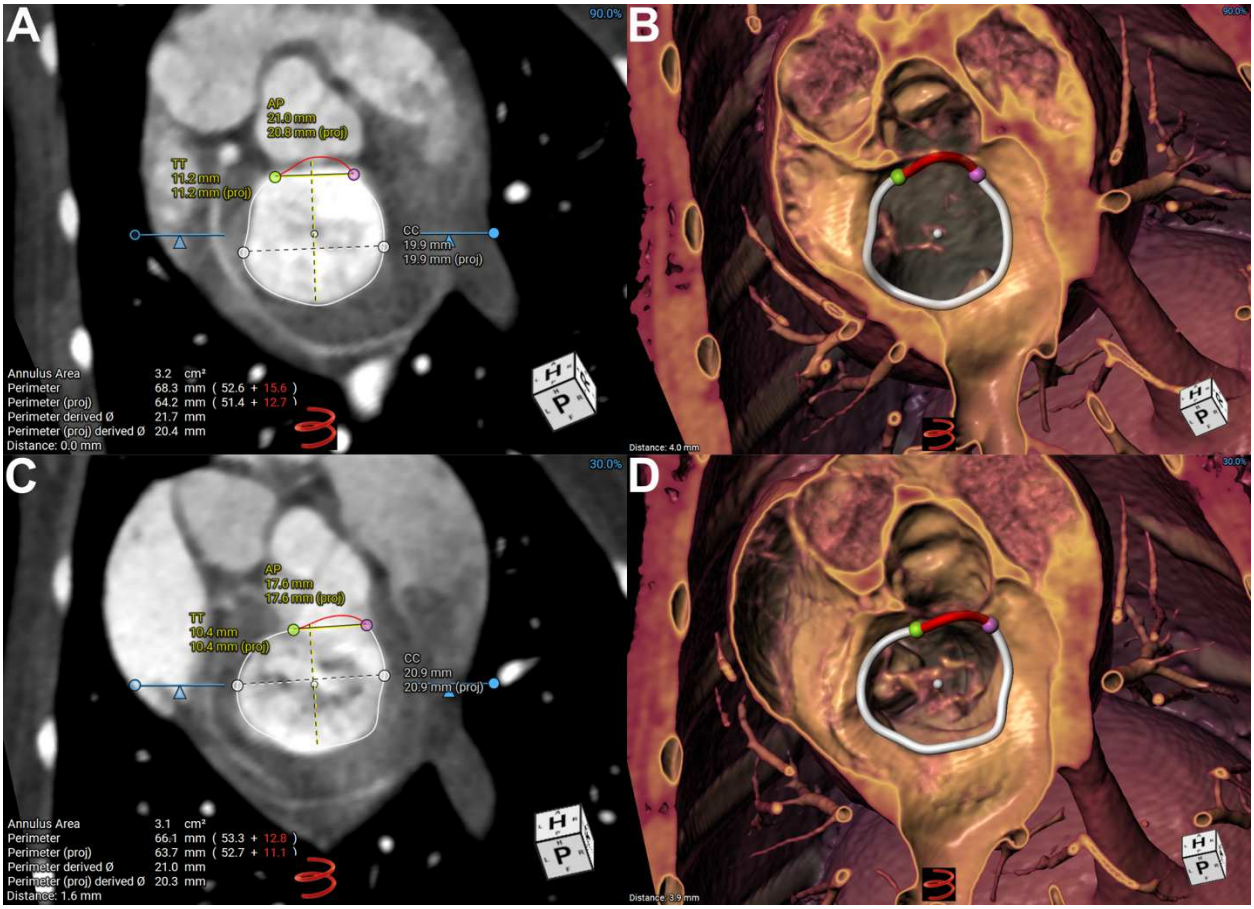

Figure 3.1: Segmentation and measurements of mitral annular geometry by cardiac computed tomography. Segmented virtual mitral annulus (MA) on multiplanar reformatting (A and C) and volume rendered (B and D) images from the atrial perspective at end diastole (A and B) and end systole (C and D). The green and pink markers were placed at the left and right fibrous trigones. The mitral annulus was separated into the aortic (red) and parietal (white) portions. AP, aortoparietal distance; CC, intercommissural distance; TT, trigone-to-trigone distance.

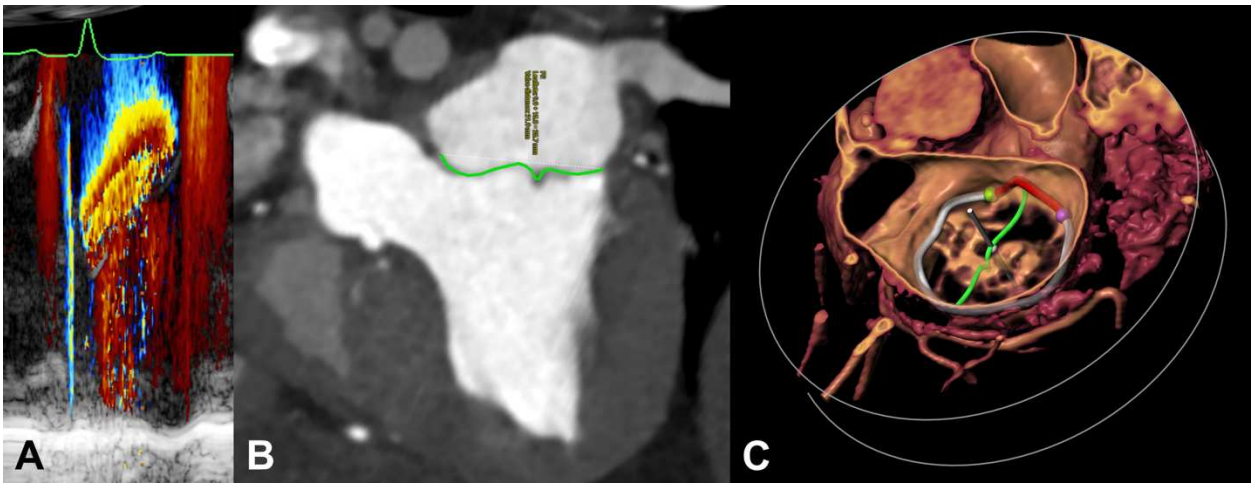

Figure 3.2: Measuring leaflet-to-annulus index (LAI) on cardiac computed tomography. The LAI was measured during the late systolic phase which is the assumed phase with peak effective regurgitant orifice area of mitral regurgitation. A: Color M-mode across the flow convergence of a mitral regurgitant jet on transthoracic echocardiogram from one of the dogs in the study. The radius of the flow convergence reaches its maximum during the latter half of ventricular systole. B: Measuring leaflet lengths (green curved lines) and aortoparietal distance (white dotted line) by cardiac computed tomography in multiplanar reformatting at the late systolic phase. C: The same LAI measurements in B on a volume rendered image of the mitral valve (left atrial perspective). The mitral annulus was segmented as described in Figure 1.

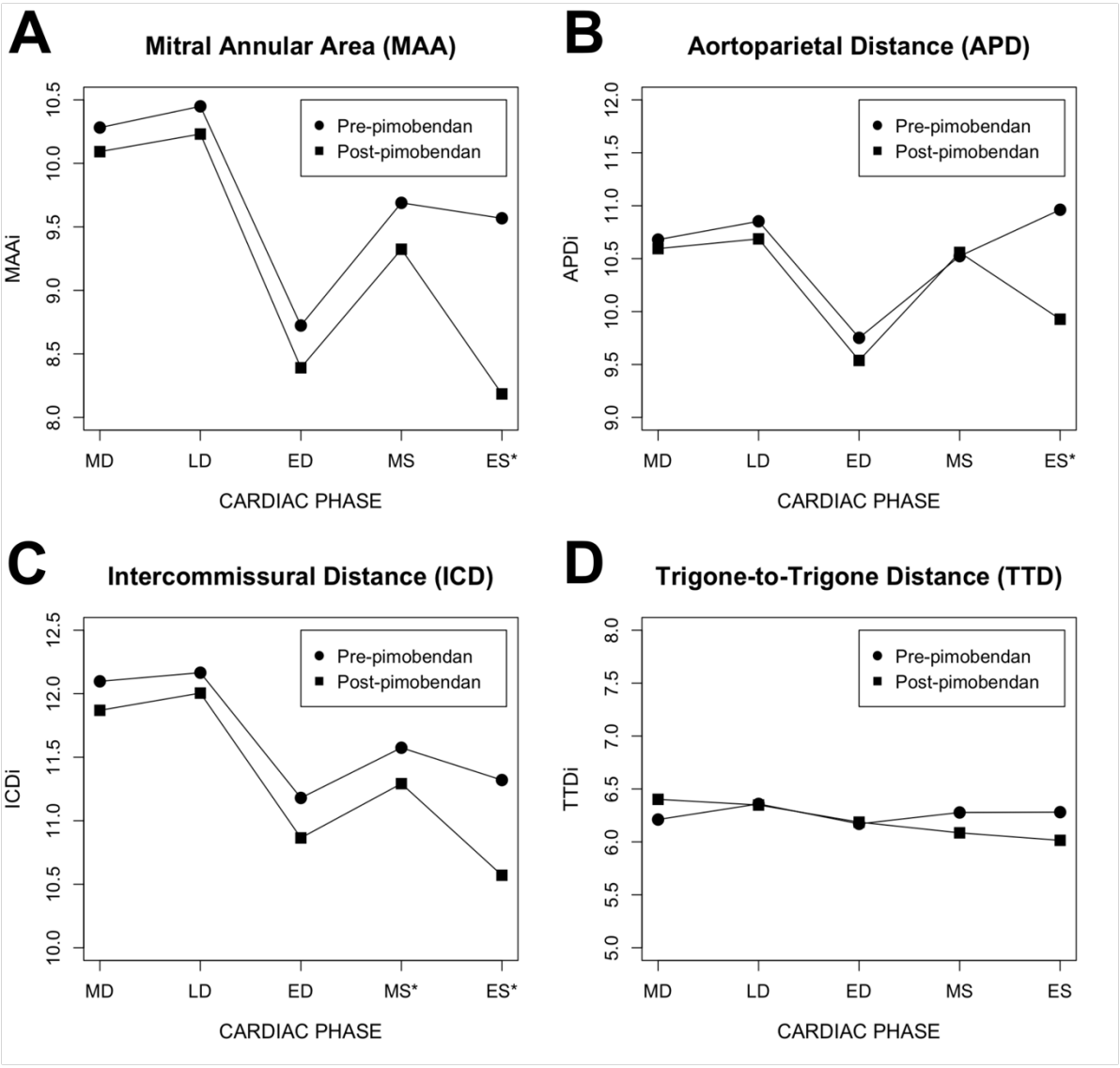

Figure 3.3: Mitral annular dynamics before and after pimobendan in dogs with ACVIM stage B2 degenerative mitral valve disease. Temporal changes in mitral annular area (A), aortoparietal distance (B), intercommissural distance (C), and trigone-to-trigone distance (D) before and after pimobendan are compared at each cardiac phase. Linear measurements were indexed to (body weight in kilograms)$^{1/3}$ and the mitral annular area was indexed to body surface area in square meters. APDi, indexed aortoparietal distance; ED, end diastole; ES, end systole; ICDi, indexed intercommissural distance; LD, late diastole; MAAi, indexed mitral annular area; MD, mid diastole; MS, mid systole; TTDi, indexed trigone-to-trigone distance. *Significant difference in measurement after pimobendan ($p < 0.05$).

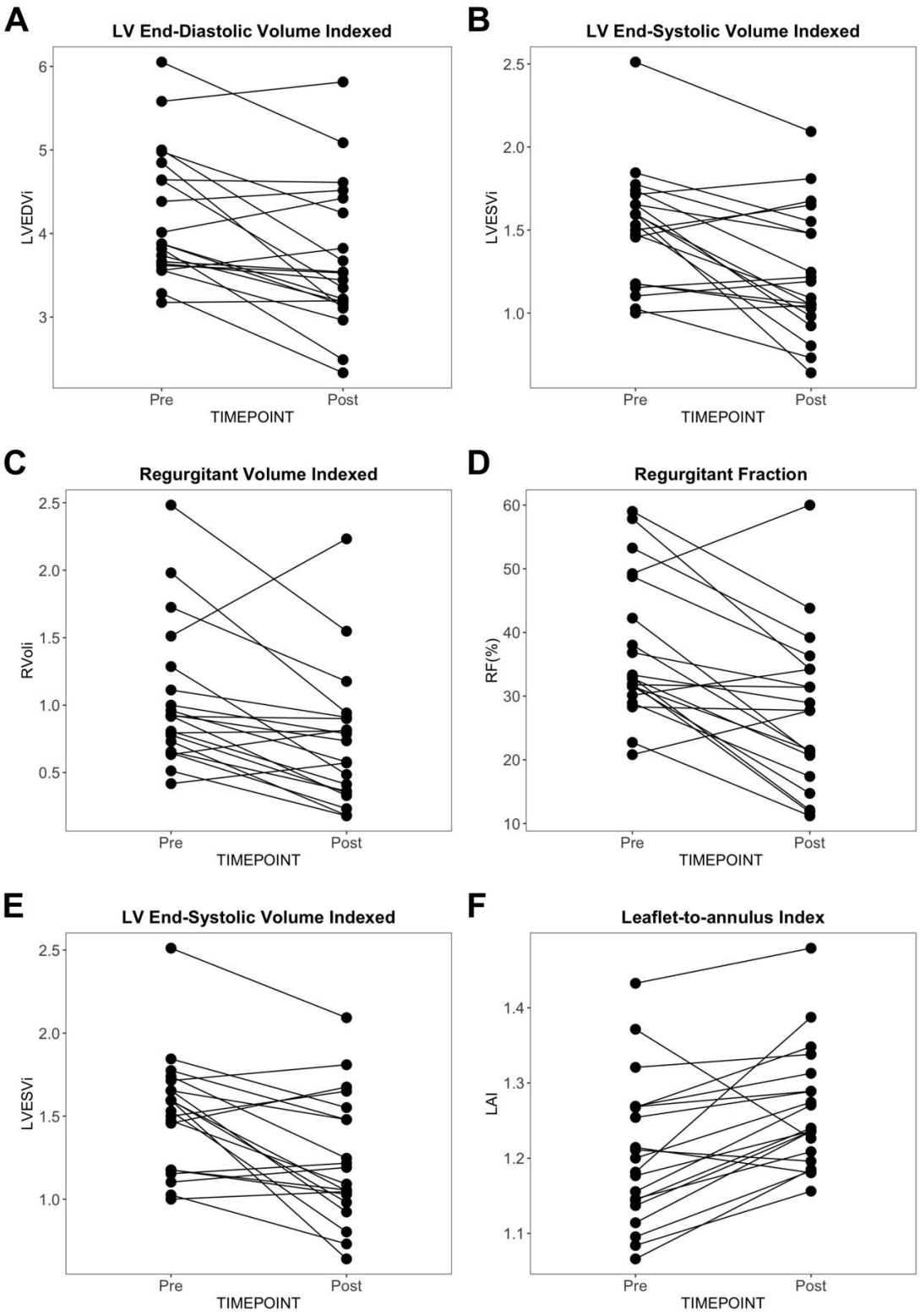

Figure 3.4: Changes in left heart volumes, severity of mitral regurgitation, and leaflet-to-annulus index after short term administration of pimobendan. Volumetric measurements are indexed to bodyweight in kilograms. All measurements decreased after pimobendan ($p < 0.05$).

REFERENCES – CHAPTER 3

[1] Boswood A, Häggström J, Gordon SG, Wess G, Stepien RL, Oyama MA, Keene BW, Bonagura J, MacDonald KA, Patteson M, Smith S, Fox PR, Sanderson K, Woolley R, Szatmári V, Menaut P, Church WM, O'Sullivan ML, Jaudon JP, Kresken JG, Rush J, Barrett KA, Rosenthal SL, Saunders AB, Ljungvall I, Deinert M, Bomassi E, Estrada AH, Fernandez Del Palacio MJ, Moise NS, Abbott JA, Fujii Y, Spier A, Luethy MW, Santilli RA, Uechi M, Tidholm A, Watson P. Effect of pimobendan in dogs with preclinical myxomatous mitral valve disease and cardiomegaly: the epic study—a randomized clinical trial. Veterinary Internal Medicine. 2016;30(6):1765–79.

[2] Ellis-Reis RE, Visser LC, Hsue W, Sharpe AN, Kaplan JL. Echocardiographic evaluation of regurgitant fraction in dogs with subclinical myxomatous mitral valve disease: Method comparison, effects of pimobendan, and reproducibility. J Vet Cardiol. 2023;45:27–40.

[3] Boswood A, Gordon SG, Häggström J, Wess G, Stepien RL, Oyama MA, Keene BW, Bonagura J, MacDonald KA, Patteson M, Smith S, Fox PR, Sanderson K, Woolley R, Szatmári V, Menaut P, Church WM, O'Sullivan ML, Jaudon JP, Kresken JG, Rush J, Barrett KA, Rosenthal SL, Saunders AB, Ljungvall I, Deinert M, Bomassi E, Estrada AH, Fernandez Del Palacio MJ, Moise NS, Abbott JA, Fujii Y, Spier A, Luethy MW, Santilli RA, Uechi M, Tidholm A, Schummer C, Watson P. Longitudinal analysis of quality of life, clinical, radiographic, echocardiographic, and laboratory variables in dogs with preclinical myxomatous mitral valve disease receiving pimobendan or placebo: the epic study. Veterinary Internal Medicine. 2018;32(1):72–85.

[4] Lombard CW, Jöns O, Bussadori CM. Clinical efficacy of pimobendan versus benazepril for the treatment of acquired atrioventricular valvular disease in dogs. J Am Anim Hosp Assoc. 2006;42(4):249–61.

[5] Mizuno T, Chen A, Mamada K, Takahashi A, Uchida S, Uechi M. Analysis of mitral valve morphology in dogs undergoing mitral valve repair with three-dimensional transesophageal echocardiography. J Vet Cardiol. 2021;34:64–72.

[6] Menciotti G, Borgarelli M, Aherne M, Wesselowski S, Häggström J, Ljungvall I, Lahmers SM, Abbott JA. Mitral valve morphology assessed by three-dimensional transthoracic echocardiography in healthy dogs and dogs with myxomatous mitral valve disease. Journal of Veterinary Cardiology. 2017;19(2):113–23.

[7] Little SH, Ben Zekry S, Lawrie GM, Zoghbi WA. Dynamic annular geometry and function in patients with mitral regurgitation: insight from three-dimensional annular tracking. J Am Soc Echocardiogr. 2010;23(8):872–9.

[8] Grewal J, Suri R, Mankad S, Tanaka A, Mahoney DW, Schaff HV, Miller FA, Enriquez-Sarano M. Mitral annular dynamics in myxomatous valve disease: new insights with real-time 3-dimensional echocardiography. Circulation. 2010;121(12):1423–31.

[9] Levack MM, Jassar AS, Shang EK, Vergnat M, Woo YJ, Acker MA, Jackson BM, Gorman JH, Gorman RC. Three-dimensional echocardiographic analysis of mitral annular dynamics: implication for annuloplasty selection. Circulation. 2012;126(11 Suppl 1):S183-188.

[10] Clavel MA, Mantovani F, Malouf J, Michelena HI, Vatury O, Jain MS, Mankad SV, Suri RM. Dynamic phenotypes of degenerative myxomatous mitral valve disease: quantitative 3-dimensional echocardiographic study. Circ Cardiovasc Imaging. 2015;8(5):e002989.

[11] Mihaila S, Muraru D, Miglioranza MH, Piasentini E, Aruta P, Cucchini U, Iliceto S, Vinereanu D, Badano LP. Relationship between mitral annulus function and mitral regurgitation severity and left atrial remodelling in patients with primary mitral regurgitation. Eur Heart J Cardiovasc Imaging. 2016;17(8):918–29.

[12] Keene BW, Atkins CE, Bonagura JD, Fox PR, Häggström J, Fuentes VL, Oyama MA, Rush JE, Stepien R, Uechi M. ACVIM consensus guidelines for the diagnosis and treatment of myxomatous mitral valve disease in dogs. Veterinary Internal Medicne. 2019;33(3):1127–40.

[13] Osuga T, Morita T, Sasaki N, Morishita K, Ohta H, Takiguchi M. Echocardiographic estimation of left ventricular-arterial coupling in dogs with myxomatous mitral valve disease. Veterinary Internal Medicne. 2021;35(1):78–87.

[14] Lee HJ, Park HJ, Song JH, Song KH. Correlation between the leaflet–annulus index and echocardiographic indices in maltese dogs with myxomatous mitral valve disease. Veterinary Sciences. 2023;10(8):493.

[15] Tabata N, Weber M, Sugiura A, Öztürk C, Ishii M, Tsujita K, Nickenig G, Sinning J. Impact of the leaflet-to-annulus index on residual mitral regurgitation in patients undergoing edge-to-edge mitral repair. JACC: Cardiovascular Interventions. 2019;12(24):2462–72.

[16] Isaka M, Hisada S, Araki R, Ueno H. The leaflet-annulus index in canine myxomatous mitral valve disease. Research in Veterinary Science. 2022;152:245–7.

[17] Oberoi S, Schoepf UJ, Meyer M, Henzler T, Rowe GW, Costello P, Nance JW. Progression of arterial stiffness and coronary atherosclerosis: longitudinal evaluation by cardiac ct. American Journal of Roentgenology. 2013;200(4):798–804.

[18] Jia C fu, Jiang Y nong, Yang Z qiang, Sun X xia, Yu Y, Wang H, Lu Y, Chen A, Wang Z. Ascending aortic elasticity and related risk factors study on prehypertension patients. American Journal of Hypertension. 2017;30(1):61–6.

[19] Sonoda M, Takenaka K, Sakamoto T, Watanabe F, Nakajima Y, Dong Yang W, Omata M. Effects of dobutamine infusion on mitral regurgitation. Echocardiography. 1998;15(1):13–9.

[20] Yoran C, Yellin EL, Becker RM, Gabbay S, Frater RW, Sonnenblick EH. Dynamic aspects of acute mitral regurgitation: effects of ventricular volume, pressure and contractility on the effective regurgitant orifice area. Circulation. 1979;60(1):170–6.

[21] Borgenhagen DM, Serur JR, Gorlin R, Adams D, Sonnenblick EH. The effects of left ventricular load and contractility on mitral regurgitant orifice size and flow in the dog. Circulation. 1977;56(1):106–13.

[22] Fox PR. Pathology of myxomatous mitral valve disease in the dog. Journal of Veterinary Cardiology. 2012;14(1):103–26.

[23] Tsakiris AG, Von Bernuth G, Rastelli GC, Bourgeois MJ, Titus JL, Wood EH. Size and motion of the mitral valve annulus in anesthetized intact dogs. Journal of Applied Physiology. 1971;30(5):611–8.

[24] Antoine C, Mantovani F, Benfari G, Mankad SV, Maalouf JF, Michelena HI, Enriquez-Sarano M. Pathophysiology of degenerative mitral regurgitation: new 3-dimensional imaging insights. Circ Cardiovasc Imaging. 2018;11(1):e005971.

[25] Rehfeldt KH, Lambert AS. Assessment of mitral regurgitation: mechanism, severity, and…timing?!? Anesthesia & Analgesia. 2016;122(2):299–301.

[26] Enriquez-Sarano M, Sinak LJ, Tajik AJ, Bailey KR, Seward JB. Changes in effective regurgitant orifice throughout systole in patients with mitral valve prolapse. A clinical study using the proximal isovelocity surface area method. Circulation. 1995;92(10):2951–8.

[27] Schwammenthal E, Chen C, Benning F, Block M, Breithardt G, Levine RA. Dynamics of mitral regurgitant flow and orifice area. Physiologic application of the proximal flow convergence method: clinical data and experimental testing. Circulation. 1994;90(1):307–22.

[28] Cobey FC, Ashihkmina E, Edrich T, Fox J, Shook D, Bollen B, Breeze JL, Sanouri Ursprung W, Shernan SK. The mechanism of mitral regurgitation influences the temporal dynamics of the vena contracta area as measured with color flow doppler. Anesthesia & Analgesia. 2016;122(2):321–9.

[29] Menciotti G, Borgarelli M, Aherne M, Camacho P, Häggström J, Ljungvall I, Lahmers SM, Abbott JA. Comparison of the mitral valve morphologies of Cavalier King Charles Spaniels and dogs of other breeds using 3D transthoracic echocardiography. Veterinary Internal Medicne. 2018;32(5):1564–9.

[30] Guo YK, Yang ZG, Ning G, Rao L, Dong L, Pen Y, Zhang T, Wu Y, Zhang X, Wang Q. Isolated mitral regurgitation: quantitative assessment with 64-section multidetector ct—comparison with mr imaging and echocardiography. Radiology. 2009;252(2):369–76.

[31] Sargent J, Connolly DJ, Watts V, Mõtsküla P, Volk HA, Lamb CR, Luis Fuentes V. Assessment of mitral regurgitation in dogs: comparison of results of echocardiography with magnetic resonance imaging. J of Small Animal Practice. 2015;56(11):641–50.

[32] Skelding A, Valverde A. Review of non-invasive blood pressure measurement in animals: Part 2 - Evaluation of the performance of non-invasive devices. Can Vet J. 2020;61(5):481–98.

CHAPTER 4: CONCLUSION AND FUTURE DIRECTIONS

This dissertation has demonstrated the versatile utility of CCT in characterizing fluoroscopic cardiac anatomy, optimizing fluoroscopic projections for transcatheter interventions, validating cardiac measurements from other imaging modalities, and investigating the mechanism of action of cardiovascular therapies in dogs. The prediction of fluoroscopic projections for individual cardiac structures represents a major step towards optimization of intra-procedural imaging which can increase procedural precision, reduce procedural time and radiation, and improve patient outcome. As a tomographic modality, CCT offers imaging insights beyond traditional 2D visualization in the assessment of PS. In cases where TTE underestimates pulmonary valve diameter, CCT becomes invaluable in accurate sizing of transcatheter devices. Finally, CCT illustrates the rectifying effect of pimobendan on abnormal mitral annular dynamics caused by mitral regurgitation. This finding explains the clinical benefit reported in major clinical trials in dogs with subclinical degenerative mitral valve disease. The capacity to measure cardiac volumes also empowers CCT to become a viable tool for the quantitative assessment of mitral regurgitation.

The future of CCT holds immense potential in veterinary cardiology, driven by the continuous advancement of transcatheter interventions and CT technology. The demand for precise peri-intervention imaging will undoubtedly expand when more sophisticated procedures such as transcatheter valve replacement become viable in dogs with congenital or acquired heart diseases. Photon-counting CT, with its superior spatial resolution, reduced radiation dose, and improved tissue characterization, will enable more detailed anatomical and functional assessment of the cardiovascular system beyond what is currently achievable by contemporary CT

platforms. The ability to better visualize and quantify myocardial perfusion and tissue composition will likely generate novel indications of CCT for the detection, monitoring, and assessment of therapeutic response in myocardial and pericardial diseases. Last but not least, initiatives to establish training and practice standards in CCT are needed to match the uprising demand and access to advanced imaging technologies in veterinary cardiology.

LIST OF ABBREVIATIONS

2D	two-dimensional
3D	three-dimensional
ACVIM	American college of veterinary internal medicine
Ao	aorta
ADI	aortic distensibility index
APD	aortoparietal distance
AL	aortic leaflet
AV	aortic valve
CAU	caudal c-arm angulation
CaVC	caudal vena cava
CC	cone of confidence
CCT	cardiac computed tomography
CI	confidence interval
CO	cusp-overlap
CP	coplanar
CRA	cranial c-arm angulation
CT	computed tomography
CrVC	cranial vena cava
DMVD	degenerative mitral valve disease
Ea	arterial elastance
ED	end diastole
EF	ejection fraction
ES	end systole
FI	female intact
FS	female spayed
FSV	forward stroke volume

IAS	interatrial septum
ICD	intercommissural distance
LA/Ao	left atrium-to-aortic dimension ratio
LAEDV	left atrial end diastolic volume
LAESV	left atrial end systolic volume
LAI	Leaflet-to-annular index
LAO	left anterior oblique c-arm rotation
LCA	left coronary artery
LD	late diastole
LV	left ventricle
LVEDV	left ventricular end diastolic volume
LVESV	left ventricular end systolic volume
LVIDdN	normalized left ventricular internal dimension in diastole
LVOT	left ventricular outflow tract
MA	mitral annulus
MAA	mitral annular area
MAD	mitral annular dynamics
MBP	mean blood pressure
MC	male castrated
MD	mid diastole
MI	male intact
MPR	multiplanar reformatting
MR	mitral regurgitation
MS	mid systole
MV	mitral valve
OFP	optimal fluoroscopic projection
PL	parietal leaflet
PS	pulmonary valve stenosis
PT	pulmonary trunk

PV	pulmonary valve
RA	right atrium
RAO	right anterior oblique
RCA	right coronary artery
RF	regurgitant fraction
RV	right ventricle
RVol	regurgitant volume
SD	standard deviation
SI	sphericity index
SOI	structure of interest
STJ	sinotubular junction
TCI	transcatheter cardiac intervention
TD	thoracic depth
TDTWR	thoracic depth-to-width ratio
TPVI	transcatheter pulmonary valve intervention
TSV	total stroke volume
TTD	trigone-to-trigone distance
TTE	transthoracic echocardiography
TLL	total leaflet length
TW	thoracic width